Understanding the chemical vapor deposition of diamond: recent progress

2009 J. Phys.: Condens. Matter 21 364201

(http://iopscience.iop.org/0953-8984/21/36/364201)

J. Phys.: Condens. Matter **21** (2009) 364201 (20pp) doi:10.1088/0953-8984/21/36/364201

Understanding the chemical vapor deposition of diamond: recent progress

J E Butler[1], Y A Mankelevich[2], A Cheesman[3], Jie Ma[3] and M N R Ashfold[3]

[1] Chemistry Division, Naval Research Laboratory, Washington, DC 20375, USA
[2] Skobel'tsyn Institute of Nuclear Physics, Moscow State University, Vorob'evy gory, Moscow 119991, Russia
[3] School of Chemistry, University of Bristol, Bristol BS8 1TS, UK

Received 5 April 2009
Published 19 August 2009
Online at stacks.iop.org/JPhysCM/21/364201

Abstract
In this paper we review and provide an overview to the understanding of the chemical vapor deposition (CVD) of diamond materials with a particular focus on the commonly used microwave plasma-activated chemical vapor deposition (MPCVD). The major topics covered are experimental measurements *in situ* to diamond CVD reactors, and MPCVD in particular, coupled with models of the gas phase chemical and plasma kinetics to provide insight into the distribution of critical chemical species throughout the reactor, followed by a discussion of the surface chemical process involved in diamond growth.

(Some figures in this article are in colour only in the electronic version)

1. Introduction

Growth of diamond by chemical vapor deposition (CVD) has become a well-established field over the last three decades [1–4]. CVD diamond materials range in grain size from ultrananocrystalline [5–7] and nanocrystalline [7–9] films, through polycrystalline plates and wafers [10, 11], to large single crystals [11–14]. The physical properties, doping and some of the applications of CVD diamond are discussed in other papers of this special issue. This paper will focus on the complex growth processes, with emphasis on recent developments since the extensive chapter on the 'Theory of Diamond Chemical Vapor Deposition' by Goodwin and Butler in 1997 [15].

The CVD process for diamond growth requires activation of the gaseous reactants, usually hydrogen and methane. For many practical reasons, two methods of activation are dominant in the field: the use of hot filaments and the use of plasmas. Over the last two decades, a basic understanding of the complex gaseous and surface processes involved in diamond CVD has been developed [15–17], with much of the knowledge derived from measurements using the hot filament method of activation [18–31]. This knowledge has been extensively reviewed [3, 4, 6, 15, 32–41] and provides a basis for the 'standard model' of diamond CVD.

Plasma-activated CVD, and particularly microwave plasma-activated CVD (MPCVD), has become dominant in both industrial and research facilities worldwide. Hence, we concentrate in this review on summarizing the recent progress in understanding diamond CVD with a particular focus on MPCVD. We shall also limit our discussion to primarily the hydrogen/hydrocarbon chemistry and consider only the growth of diamond on previously existing diamond surfaces, i.e. we leave the discussion of nucleation phenomena and seeding of non-diamond substrates to other works [36, 42–44]. The role of oxygen [45], nitrogen [46], halogen [47] and other chemistries [48–50] can be important in some situations, but are not required for the basic understanding of diamond growth, and can be viewed as a perturbation of the hydrogen/hydrocarbon chemistries.

The 'standard model' of diamond CVD has the following key elements. First, the diamond lattice is stabilized and prevented from rearrangement to graphitic carbon by termination with hydrogen atoms (or similar chemical species), and the temperature is too low for spontaneous bulk rearrangement to occur (i.e. below the Debye temperature of diamond). Secondly, the gaseous activation process dissociates molecular hydrogen into atoms which react with the source hydrocarbon and create a complex mixture of hydrocarbon species including reactive carbon-containing radicals. The H atoms created by the gaseous activation process also abstract hydrogen from the surface CH bonds, thereby creating surface radical sites. These radical sites will occasionally react with

gas phase carbon-containing radicals, resulting in an adsorbed carbon species. Much more frequently, however, the radical sites are simply refilled by recombining with gaseous H atoms. As discussed in more detail later, this constant turnover of the surface-terminating species (hydrogen) further drives the surface chemistry to dehydrogenate the adsorbed carbon species and to incorporate carbon into the lattice. Finally, the atomic hydrogen, and, to a lesser extent, other gaseous species, react with any sp or sp^2 carbon sites on the surface, converting them into sp^3 bonded carbon. This 'standard model' of diamond CVD was developed by contributions from many authors and is summarized in the 1993 Butler and Woodin article [17] and the 1997 Goodwin and Butler review chapter [15].

2. Gas phase processes in microwave-assisted CVD

The vital roles of H atoms in activating and cycling hydrocarbon species within the process gas mixture were highlighted above. Consider the case of CH_4, the most commonly used hydrocarbon source gas. H atoms drive the series of fast 'H-shifting' reactions (1) involving, in the hot regions, abstractions:

$$CH_y + H \rightleftharpoons CH_{y-1} + H_2, \qquad y = 4\text{–}1 \qquad (1a)$$

and, in the cooler regions, additions of the type

$$CH_{y-1} + H + M \rightleftharpoons CH_y + M \qquad y = 4\text{–}1 \qquad (1b)$$

(where M is a third body). The relative densities of the various CH_y ($y \leqslant 4$) species depend on the local H atom density and gas temperature, T_{gas}, and thus show a wide spatial variation. T_{gas}, for example, can be ~3000 K within the plasma ball in an MPCVD reactor, yet not much above room temperature close to the reactor walls. C_2H_x species are formed by CH_y radical recombinations:

$$CH_x + CH_y + M \rightleftharpoons C_2H_{x+y} + M \qquad (2a)$$

$$CH_x + CH_y \rightleftharpoons C_2H_{x+y-1} + H \qquad (2b)$$

$$CH_x + CH_y \rightleftharpoons C_2H_{x+y-2} + H_2 \qquad (2c)$$

e.g.

$$CH_3 + CH_3 + M \rightleftharpoons C_2H_6 + M \rightleftharpoons C_2H_5 + H, \text{ etc.}$$

Once created, C_2H_x species can also cycle through a series of gas phase H-shifting (abstraction and/or addition) reactions analogous to (1*a*) and (1*b*), with C_2H_2 the thermodynamically favored hydrocarbon at high T_{gas} [40]. Similar recombination and H-shifting reactions can lead to the formation of C_nH_x species ($n > 2$). Such species gain in relative abundance as the carbon mole fraction in the input gas mixture is increased.

Given that all MPCVD reactors contain steep T_{gas} gradients, it follows that the total gas phase number densities, the H atom densities, the various CH_y and C_2H_x species densities, and thus the reaction rates for inter-conversion between these species, are all sensitive functions of location within the reactor. This complexity is further compounded by gas–surface reactions (at the growing diamond surface and at the walls of the reactor) and by gas transport which, in MPCVD reactors, is largely diffusive, and thus mass (and species) dependent. Recent progress towards unraveling this complexity has been driven by a combination of (laser-based) *in situ* gas phase diagnostic measurements and modeling—much of which has been performed at LIMHP, Université Paris-Nord and by the Bristol–Moscow team. Many of the key findings from these studies are summarized below.

2.1. Recent optical diagnostics

Most recent experimental advances in the diagnosis of plasmas used for diamond CVD derive from the increased flexibility of laser absorption spectroscopy methods. In favorable circumstances these enable spatially resolved determinations of the absolute column densities of selected species as functions of process conditions (e.g. applied MW power, P, the total pressure, p, and the partial pressures (flow rates) of the various input gases). Stable hydrocarbon species like CH_4, C_2H_2 and C_2H_6, and CH_3 radicals, have been monitored by direct line-of-sight infrared (IR) absorption methods using tunable diode lasers [18, 51–55] and/or quantum cascade lasers [56, 57]. CH_3 radicals have also been monitored by resonance-enhanced multiphoton ionization (REMPI) [27, 30] and line-of-sight absorption in the ultraviolet (UV) [52, 58], but most recent measurements [59–61] of radical species in MW-activated hydrocarbon/H_2 gas mixtures have employed pulsed tunable dye lasers and an alternative absorption technique—cavity ring down spectroscopy (CRDS) [62].

Absorption methods can offer major advantages if diagnosis employs a well-characterized spectroscopic transition. With due care, analysis can provide *absolute* densities of the species of interest. What is actually measured, however, is the absorption associated with the chosen probe transition. Even in the case of a homogeneous gas sample, the conversion of such a line integrated absorption (LIA) into an absolute column density requires detailed knowledge of the relevant spectroscopy and the transition moment at the appropriate gas temperature. The species number density can then be obtained by dividing the derived column density by the column length. The necessary spectroscopic data are available for some of the stronger fundamental IR absorptions of stable hydrocarbons like CH_4 and C_2H_2 through, for example, the HITRAN database [63]. For radical species, however, this has to be calculated from the integrated transition probability (determined from the Einstein A coefficient, for example) and proper consideration of rovibrational line strengths, partition functions, etc. For an inhomogeneous sample, such as that probed by any line-of-sight measurement involving an MPCVD reactor, the situation is significantly more complex, since the probed column spans a very wide range of T_{gas}. The total number density in the reactor center is typically an order of magnitude lower than that at the edge of the reactor, and the gas chemistry and composition vary hugely along the probed column. Any detailed understanding of the gas phase chemistry underpinning diamond CVD thus requires complementary experiments and theory. Experimental measurements (e.g. spatially resolved LIA measurements

as functions of process conditions) are essential for validating model calculations, but model outputs (e.g. the spatial variation of T_{gas} and of the various species mole fractions) are also essential for quantitative interpretation of the experimental data.

IR column density measurements of MW-activated hydrocarbon/H_2 gas mixtures [57] reveal efficient conversion of any input hydrocarbon (including C_2H_2) into CH_4 under the (relatively) high H atom densities, [H], and low T_{gas} conditions found where the process gas enters the reactor. Such measurements also serve to highlight the consequences of the massive variation in T_{gas} along the probed column. Since the total number density is largest and the rovibrational partition functions smallest at low T_{gas}, CH_4 and C_2H_2 molecules at the ends of the column (i.e. in the cool periphery of the reactor) dominate the measured IR absorptions; measurements of these species thus provide no direct probe of the hot plasma region itself. Nonetheless, such measurements are extremely valuable for testing, tensioning and validating predictions from complementary two-dimensional (2D) modeling studies [51, 64, 65] (see later). The combined experimental and modeling analysis leads us to visualize the reactor volume in terms of three nested regions that reflect the sensitivity of $CH_4 \leftrightarrow C_2H_2$ inter-conversion to the local T_{gas} and [H]. $CH_4 \rightarrow C_2H_2$ conversion occurs most efficiently in an annular shell around the central plasma region (henceforth **B**, characterized by 1400 K $< T_{gas} <$ 2200 K). Analysis of the multi-step $CH_4 \rightarrow C_2H_2$ conversion in this region reveals a substantial net consumption of H atoms. C_1H_x and C_2H_y species inter-convert very rapidly in the hot plasma region itself (henceforth termed region **A**), but the net conversion rates are negligible and C_2H_2 is deduced to account for >97% of the total carbon in the plasma ball. The reverse $C_2H_2 \rightarrow CH_4$ transformation is favored in regions where $T_{gas} <$ 1400 K, i.e. the periphery of the reactor (region **C**). This $C_2H_2 \rightarrow CH_4$ conversion is driven by H atoms, but involves no net consumption of H atoms [65].

The radical species are localized in the hot plasma region **A**. Figure 1 shows three measures of the ways in which three such transient species C_2 and CH radicals, and electronically excited H atoms, vary as functions of height, z, above the surface of an Mo substrate in an MPCVD reactor operating in Bristol under the 'standard' conditions defined in the caption. The column densities of $C_2(a)$, CH(X) and H($n = 2$) species are each sensitively dependent on the C/H ratio in the input process gas mixture but, as figure 1(a) shows, replacing the standard CH_4 feed ($F(CH_4) = 25$ standard cubic centimeter per minute (sccm)) by an equivalent carbon flow rate in the form of C_2H_2 ($F(C_2H_2) = 12.5$ sccm) yields identical column densities and distributions for all three species—confirming, directly and definitively, that the diamond CVD process itself is insensitive to the particular choice of carbon source gas [18, 61]. All three distributions peak away from the substrate, reflecting the surface-induced fall in T_{gas} and [H] as $z \rightarrow 0$, but the radical distributions clearly peak at larger z than that of the excited H atoms. The distributions of the former species are determined by thermal chemistry; their respective peaks reflect the spatial distribution of T_{gas}. The T_{gas} distribution controls the distribution of ground ($n = 1$) state H atoms also, but the excited H($n = 2$) atoms monitored by CRDS are formed by electron impact excitation of H($n = 1$) atoms. The spatial distribution of H($n = 2$) atoms is thus a convolution of the H($n = 1$) and electron density and temperature (n_e and T_e) distributions. As figure 1(b) shows, the recent 2D modeling of the Bristol MPCVD reactor succeeds in capturing the spatial profiles of these transient

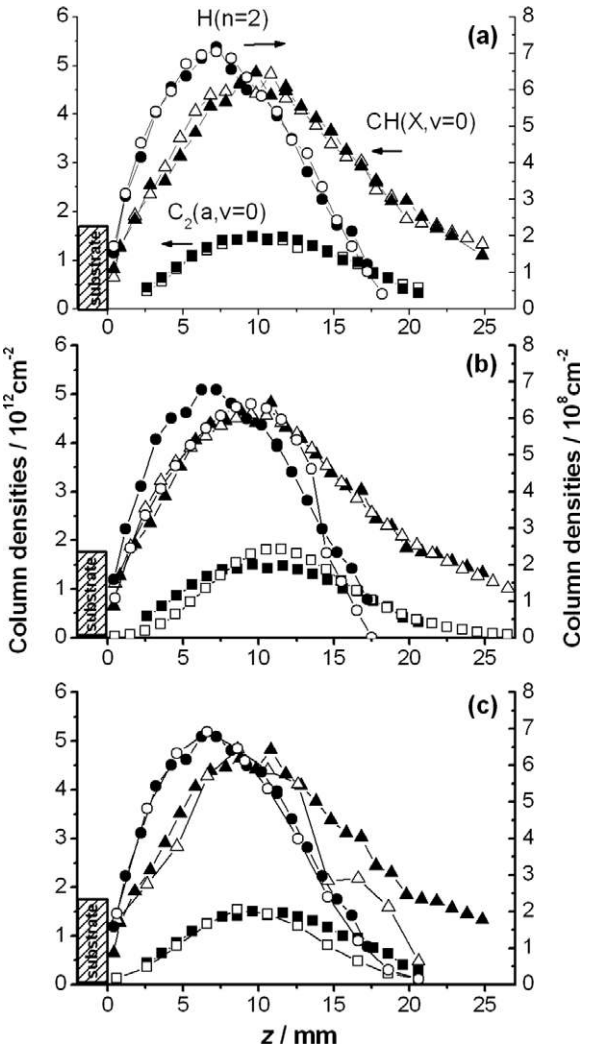

Figure 1. Plots illustrating the variation of C_2, CH and electronically excited H atom densities (right-hand scale) as a function of height, z, above a Mo substrate in the Bristol MPCVD reactor operating under the following 'base' conditions: $P = 1.5$ kW, $p = 150$ Torr, $F(CH_4) = 25$ sccm, $F(Ar) = 40$ sccm and $F(H_2) = 500$ sccm. (a) Column densities of C_2 (a, $v = 0$) and CH(X, $v = 0$) radicals (left-hand scale) and H($n = 2$) atoms (right-hand scale) measured by CRDS under base conditions (solid symbols) and with $F(CH_4)$ replaced by $F(C_2H_2) = 12.5$ sccm (and $F(H_2) = 512.5$ sccm to maintain the same total flow rate (open symbols)). (b) Measured z-dependent (by CRDS, solid symbols) and calculated (by 2D model, open symbols) $C_2(a, v = 0)$, CH(X, $v = 0$) and H($n = 2$) column densities for the base operating conditions. (c) Comparison between OES-measured $C_2(d)$, CH(A) and H_α profiles (open symbols) and CRDS-determined $C_2(a, v = 0)$, CH(X, $v = 0$) and H($n = 2$) column density profiles (solid symbols). Each OES dataset has been scaled vertically, by an appropriate factor, to emphasize the similar spatial dependences revealed by OES and CRDS.

species, quantitatively; the modest discrepancy in the H($n = 2$) profile could easily be accommodated by small adjustments to the electron density and temperature distributions used in the modeling. Such quantitative agreement between experiment and model predictions with regard not just to the respective column densities but also the local T_{gas} (as determined, experimentally, by analysis of relative line intensities and/or linewidths) lends confidence to the predicted column densities for all other C_1H_x and C_2H_y species in the immediate vicinity of the growing diamond surface. These latest model outputs support the consensus view [15, 17, 40] that CH_3 is the dominant carbon-containing radical at $z \sim 0.5$ mm, with a density $\sim 10^{14}$ cm^{-3} under the base conditions defined in the caption to figure 1. Here it is necessary to add a note of caution. Such models include terms for the loss of gas phase species (e.g. H atoms and CH_3 radicals) to the growing diamond surface, but rarely allow for other possible modifications of the gas phase composition in the boundary layer as a result of collisions with the diamond surface.

Laser absorption spectroscopy methods enable quantitative diagnosis of plasmas, including those used in diamond CVD but, in favorable cases, the simplicity, and the spectral and spatial resolution offered by optical emission spectroscopy (OES), means that this technique will be a useful supplementary diagnostic—capable of offering additional information. OES has long been recognized as a valuable technique for monitoring and optimizing plasma processes because of its high sensitivity and flexibility in operation [59, 66–77]. OES measures the emission from excited states of species, which are normally formed by electron impact excitation of the corresponding ground state species. The emission intensities are thus closely linked with the properties of electrons in the plasma. As a result, OES measurements can provide valuable information about T_e and n_e, and their variation with changes in process condition [68, 75, 76]. High resolution OES measurements can also provide estimates of the temperature of the emitting species—either through the measured Doppler broadening of a single spectral line (such as the H Balmer-α line [68, 71] or the $Q(1)$ line of the $(0, 0)$ band of the H_2 Fulcher system [71]) or from the relative intensities of a series of rotational lines (e.g. in H_2) [69, 71]. These excited state temperatures are often treated as a proxy for the local gas temperature [68, 69, 71]. OES measurements also offer a route to determining the relative densities of H($n = 1$) atoms in the MW plasma—a quantity that is rather difficult to determine by laser absorption or REMPI techniques. The method, called actinometry, depends on the presence within the plasma of a small, known amount of an inert tracer species (usually Ar) which has similar energetics for the emitting electronic state and thus probes a similar portion of the electron energy distribution in the plasma. Variations in the density of interest (here that of the H($n = 1$) atoms), and thus in the H_2 dissociation fraction, can be followed by comparing the relative intensities of the emissions from the electronically excited H and Ar atoms formed by electron impact excitation [67, 70, 71, 73–76].

Many OES studies of diamond growing plasmas have been reported, but most were performed under relatively low pressure and power density conditions and only a few [59, 72] were designed to allow careful comparison with absolute species densities measured by absorption. The validity of OES as a quantitative diagnostic at pressures relevant to most MPCVD diamond growth thus still remained a concern, but recent systematic, spatially resolved OES measurements in the Bristol MPCVD reactor have served to allay many of these anxieties [76]. Figure 1(c) compares the z-dependent $C_2(a)$, CH(X) and H($n = 2$) column densities (from CRDS) with the corresponding $C_2(d \rightarrow a)$, CH($A \rightarrow X$) and H($n = 3 \rightarrow 2$) OES intensities measured under the same process conditions. Each OES profile has been scaled, vertically, to emphasize the similarities of the respective z dependences returned by the two methods. Clearly, OES captures the H($n = 2$) profile well, but under-samples the relative densities of both radical species at large z. This is understandable. The H($n = 2$) and H($n = 3$) states monitored, respectively, by CRDS and by OES both arise as a result of electron impact excitation of ground state H($n = 1$) atoms; the spatial distributions of both excited state species are thus determined by essentially the same convolution of H($n = 1$) and electron densities. The $C_2(a)$ and CH(X) densities, in contrast, are almost entirely determined by thermal chemistry in the hot plasma region, and only their excited state densities are sensitive to the electrons. The reduced detection of these species in the OES measurements at large z thus reflects the associated fall in n_e (and T_e) in this region. The small amount of Ar present in the process gas mixture serves as a useful actinometer—offering a route to determining relative concentrations of H($n = 1$) atoms, and their variation with process conditions.

Optical diagnosis of diamond growing plasmas has progressed considerably in the past few years. The most recent families of studies, involving quantitative, spatially resolved monitoring of several different species as functions of a wide range of process conditions, in concert with complementary reactor modeling studies, are providing a much improved picture of the gas phase chemistry and composition that underpins diamond CVD. Extensions to B-containing gas mixtures, such as are used for growth of B-doped diamond, are now underway [78, 79]. As mentioned above, the gas compositional changes in the boundary layer through collisions at the substrate surface would benefit from further investigation, but the main future challenge lies in exploiting this improved knowledge of the gas phase chemistry into more accurate, realistic and predictive models of the gas–surface interactions involved in diamond CVD. Recent progress in this area is summarized in section 3 of this paper.

2.2. *Plasma modeling*

Modeling studies reported over the past two decades have provided progressively greater understanding and allowed optimization of diamond deposition processes in relatively simple hot filament CVD reactors [25, 80–85], in dc arc jet reactors [86] and in MPCVD reactors [53, 65, 87–97]. The latter environment is considerably more challenging; many complex and interrelated phenomena require careful consideration in order to achieve an adequate simulation of the diamond deposition processes occurring in an MW PECVD

reactor. These include: the propagation of electromagnetic fields in the reaction chamber and their interaction with the plasma; gas heating; heat and mass transfer; a plethora of charged and neutral species involved in the huge array of plasma-chemical reactions for real source gas mixtures (i.e. H/C or H/C/noble gas mixtures); the non-equilibrium electron energy distribution; radiation processes; species diffusion and thermodiffusion; and a range of gas–surface processes. To accommodate all of these processes in a self-consistent manner is a problem of extreme complexity. Thus, various simplifications have been used in all such models developed over the past decade—e.g. 2D models including realistic treatment of the electromagnetic field but restricted to the case of pure H_2 [87–91], 2D models for H/C mixtures [92] and for H/C/Ar [65, 93, 94] mixtures but without explicit calculation of the electromagnetic fields, and various 1D models (in the axial z and radial r directions) for H/C [64, 95, 97] and H/C/Ar [53] mixtures.

1D models involving real process gas mixtures can serve as good tools for studying plasma-chemical processes. 2D models involving pure H_2 can be used to investigate peculiarities of plasma–field interactions and heat and mass transport. Consideration of the various model outputs allows one to formulate the key requirements of any model designed to allow for quantitative predictions and characterization of the diamond deposition processes. Such a model should be realized in (at least) a 2D coordinate system, e.g. (r, z) in the case of a reactor with cylindrical symmetry, and it should provide reliable predictions of the T_{gas} distributions (and thus of the power absorption and balance), of the atomic H and hydrocarbon species concentrations, and of the various fluxes on the substrate. Given the uncertainties and the lack of information concerning many of the elementary processes, plasma-chemical kinetics, etc, such models should ideally be tested and validated against a large body of (spatially resolved) experimental data obtained via systematic variation of a range of reactor parameters.

One aim of a comprehensive combined experimental [57, 61, 76, 96]/theoretical study [57, 61, 65, 96] was to develop and test the advanced 2D model of MPCVD reactors operating with H/C, H/C/Ar or H/C/He process gas mixtures and used for UNCD [94, 96], MCD [57, 61, 65, 76, 79] and SCD (single-crystal diamond) [92, 94] deposition. Here we present the essence of the MPCVD reactor modeling [65], highlighting the key difficulties and some of the advantages of using a 2D representation, and summarize selected key insights that emerge from modeling the plasma-chemical processes prevailing in such an MPCVD reactor when operating under conditions typical for MCD deposition from H/C/Ar gas mixtures at pressures $p = 75$–150 Torr and input powers $P = 1$–1.5 kW.

The main model blocks are incorporated in a self-consistent manner [65] and describe:

(i) power absorption and gas heating, heat and mass transfer;
(ii) plasma activation of the reactive gas mixture, the plasma-chemical kinetics involving calculation of non-equilibrium electron energy distribution functions (EEDFs), diffusion and thermal diffusion of neutral species; ambipolar diffusion of the charged species, and
(iii) gas–surface processes (diamond deposition, loss/production of radicals, ions and electrons).

The surface kinetics block (iii) handles the reactions of hydrocarbon species as well as H and molecular H_2 with a solid (at the substrate and substrate holder), and recombination of H at the chamber walls. Gas–surface reactions include H abstraction to form radical surface sites and the subsequent reactions of these sites with H, H_2 and hydrocarbon radicals. The main effect of these reactions is to reduce the H atom densities directly above the growing diamond surface and the surface of the substrate holder. Such reductions can be substantial in typical MPCVD conditions. For example, the calculated H atom density at the substrate surface, [H] ($z = 0$) $\sim 2 \times 10^{15}$ cm^{-3}, is only a quarter of that 0.5 mm above the surface, [H] ($z = 0.5$ mm) $\sim 8 \times 10^{15}$ cm^{-3} [65] as illustrated below (figure 2).

The rate coefficients of the various plasma activation reactions (i.e. electron–atom and electron–molecule reactions) depend on the local EEDF which, under typical MPCVD reactor conditions, is a function of the reduced electric field E/N [65]. The 2D modeling [65] summarized here does not include explicit calculation of the electromagnetic fields: rather, it introduces the two simplifying assumptions. First, E/N and the average electron temperature T_e both tend to be distributed rather uniformly throughout the whole plasma region, except at the plasma edge (the boundary shell). Thus it is assumed that the steep exponential dependences of the ionization rates and the electron density on E/N ensure that only a narrow range of E/N values will be realized in a MW plasma excited by any given input power density. Support for this assumption is provided by previous calculations of the electromagnetic fields and plasma parameters for pure hydrogen plasma [87–89]. Second, the size of the plasma region used in the model (i.e. its radius r_{pl} and height h_{pl} in the case of a cylindrical plasma volume) is treated as an external parameter, guided by experimental absorption and/or optical emission spectroscopy data. These simplifications allow the MW power absorption and the activation volume to be accommodated as parameters within the model blocks, and thus allow estimation of E/N and T_e in the plasma region for a given value of input power. The absorbed power density is calculated directly as a sum of power losses and gains associated with the various electron–particle reactions (e.g. electronic, vibrational and rotational excitation/de-excitation, dissociation, ionization).

The extreme range of conditions (e.g. T_e, radical and charged species densities) prevailing in different regions of the MPCVD reactor dictates that a rather comprehensive plasma-chemical mechanism needs to be used in any advanced models. The plasma-chemical kinetics mechanism [65] used in the recent Bristol/Moscow modeling includes more than 240 direct and reverse reactions involving 30 neutral species and 8 charged species (electrons, and the ions $C_2H_2^+$, $C_2H_3^+$, H^+, H_2^+, H_3^+, Ar^+ and ArH^+); this mechanism was further extended when modeling the gas phase chemistry prevailing in UNCD deposition conditions (i.e. 1%CH_4/2%H_2/97%Ar) by the inclusion of additional ions (C^+, C_2^+, C_3^+, CH^+, C_2H^+ and C_3H^+).

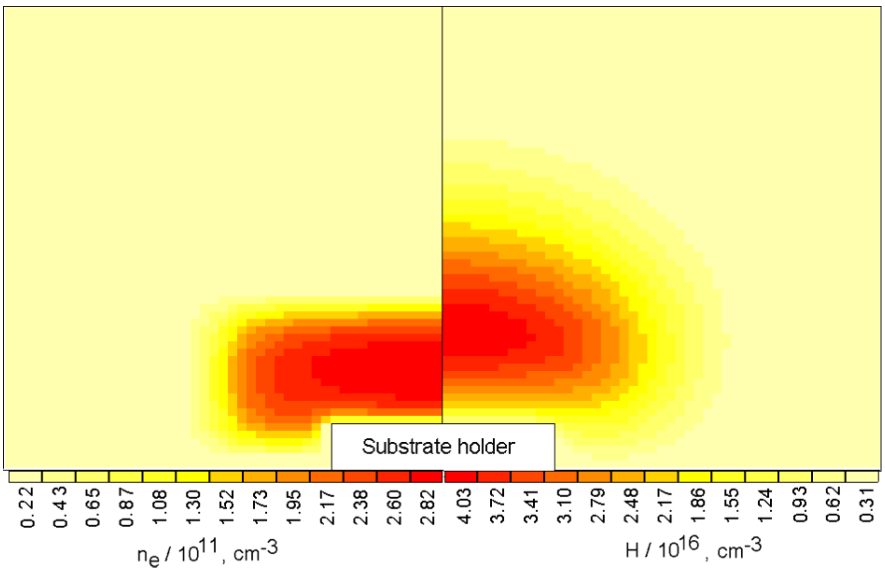

Figure 2. 2D (r, z) plots of the calculated (left) electron and (right) H atom concentrations, for substrate holder diameter $d_{sh} = 3$ cm and input power $P = 1.5$ kW. From the edge of the chamber to the center the color scale increases in 13 equal intervals, e.g. from 0–0.22 $\times$ 10^{11} to 2.60 $\times$ 10^{11}–2.82 $\times$ 10^{11} cm^{-3} (left), and from 0–0.31 $\times$ 10^{16} to 3.72 $\times$ 10^{16}–4.03 $\times$ 10^{16} cm^{-3} (right).

At the final stage of model development, the set of model equations needs to be solved in a self-consistent manner [65]. The non-stationary conservation equations for mass, momentum, energy and species concentrations are solved numerically by a finite difference method in (r, z) coordinates to provide spatial distributions of T_{gas}, species concentrations, power absorption and transfer channels as functions of reactor operating conditions. The 2D model takes account of changes in plasma parameters and conditions (e.g. in T_{gas}, T_e, the electron density (n_e), the power density and the plasma chemistry) induced by varying reactor parameters like p, P, and the mole fractions of CH_4 and Ar in the process gas mixture. Typical values for the plasma parameters in the plasma core returned by the 2D model are [65]: $T_{gas} \sim$ 2800–2950 K, power densities 20–40 W cm^{-3}, reduced electric fields $E/N \sim$ 25–30 Td, $n_e \sim$ (2–3) $\times$ 10^{11} cm^{-3} and H atom mole fraction $X_H \sim$ 8% for the base conditions defined in the caption to figure 1—i.e. $p = 150$ Torr, $P = 1.5$ kW, $F(CH_4) = 25$ sccm, $F(Ar) = 40$ sccm and $F(H_2) = 500$ sccm, with a substrate diameter $d_s = 3$ cm and temperature $T_s = 973$ K, a model reactor chamber of diameter $d_r = 12$ cm and height $h = 6$ cm, and the following external parameters: cylindrical plasma bulk with radius $r_{pl} \sim 2.9$ cm and height $0 < z < h_{pl} = 1.4$ cm, and $T_e \sim 1.28$ eV. Figure 2 shows 2D (r, z) false-color plots depicting the electron and H atom number density profiles returned for these conditions. The right panel of figure 2 clearly shows the large fall in [H] at small z highlighted previously (reflecting H atom loss by reaction at the substrate surface and the rapid decline in the local T_{gas}).

We now consider the main plasma-chemical processes occurring in MPCVD reactors as revealed by the model outputs for the above base reactor conditions [65]. The absorbed power density within the plasma volume declines with increasing z, from ~47 W cm^{-3} at $z \sim 2$ mm above the substrate center to ~30 W cm^{-3} in the center of the hot region (at $z \sim 10$ mm). The major fraction (>90–95%) of the MW power absorbed by the electrons is expended in vibrational and rotational excitation of gas phase molecules (H_2 and C_xH_y). The input power absorbed at the center of the plasma core ($r = 0$, $z \sim 10$ mm) is typically partitioned as follows: ~66% into vibrational (V) excitation, ~27% into rotational (R) excitation of H_2, and ~ 5% is lost through elastic collisions between electrons and H_2 molecules. About 1.6% of the absorbed power is consumed in dissociating H_2 molecules following excitation to triplet states. The remainder goes into excitation, dissociation and ionization of different gas species. A significant part of the e-V and e-R excitation energy is dissipated as gas heating via rotational–translational (R–T) and vibrational–translational relaxation (e.g. V–T relaxation of $H_2(v)$ molecules in collisions with H atoms). As a result, much of the e-V excitation energy is ultimately partitioned into H atom kinetic energy—thereby providing a source of translationally excited ('hot') H atoms that might be detectable if the V–T relaxation rate is comparable with the fast rates of elastic collisions of H atoms with H_2 molecules and other particles. Subsequent collisions between the excited neutral particles and ground state molecules and atoms in the background gas lead to this excess energy becoming redistributed throughout the plasma ball and cause it to heat to $T_{gas} \sim 2930$ K. A proper treatment of H_2 rotational and vibrational excitation (by electron impact) and of the subsequent V–T and R–T relaxation processes is essential for obtaining a reliable prediction of T_{gas}.

Thermal dissociation of H_2 is the major source of H atoms at high temperatures ($T_{gas} \geqslant 2800$ K) and, under the defined base conditions, is at least an order of magnitude more important than electron impact dissociation of H_2 molecules. However, the relative contribution to the H atom density from plasma sources can be very process-dependent [98] and becomes increasingly significant with increasing argon dilution. Indeed, simulations of UNCD deposition in MPCVD

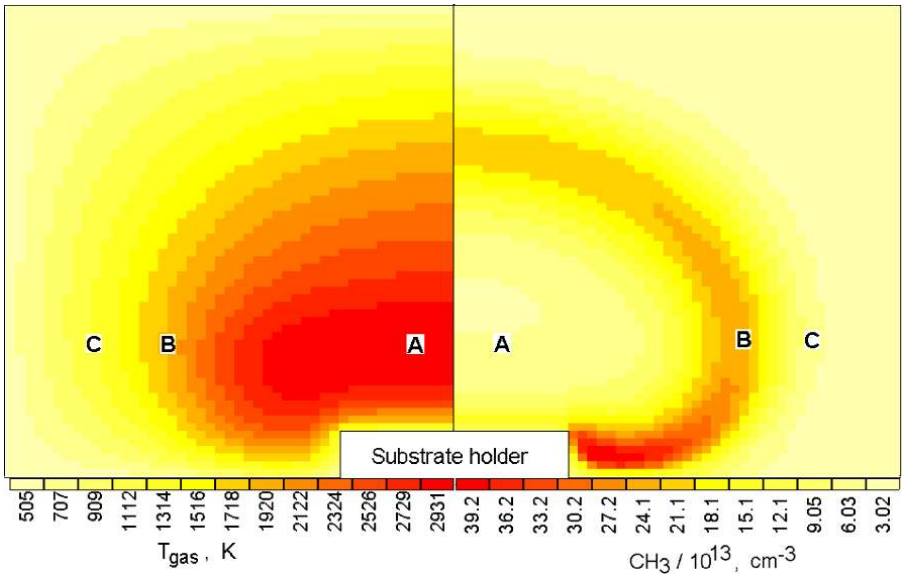

Figure 3. 2D (r, z) plots of the calculated (left) gas temperature, $T_{\rm gas}$, in kelvin and (right) CH_3 number density, for substrate holder diameter $d_{\rm sh} = 3$ cm and input power $P = 1.5$ kW. The color scale increases in 13 equal intervals, e.g. from 303–505 to 2729–2931 K (left), and from 0–3.02×10^{13} cm^{-3} to 3.62×10^{14}–3.92×10^{14} cm^{-3} (right).

reactors show that plasma sources dominate at high $X_{\rm Ar}$ and can provide extremely high degrees of dissociation (e.g. $X_{\rm H} \sim 2.6\% \gg X_{\rm H2} \sim 0.16\%$) [94].

The main ionization processes under the defined base plasma conditions are electron impact ionization of C_2H_2, H_2 and H, and the associative ionization reaction between H($n \geqslant 2$) atoms and H_2 molecules. H_3^+ is the most abundant ion in a pure Ar/H_2 plasma. The model does not allow for possible conversion to more complex ions (e.g. H_5^+, $C_xH_y^+$), which would introduce some changes in electron–ion recombination rates and in ambipolar diffusion, but such neglect is not expected to introduce any fundamental changes to the plasma density or the reported results. H_3^+ is rapidly usurped by $C_2H_2^+$ and $C_2H_3^+$, however, upon addition of even small amounts of hydrocarbons. Thermal processing ensures that C_2H_2 is the most abundant hydrocarbon species in the base plasma. It has a much lower ionization potential ($I_{\rm C2H2} = 11.4$ eV) than H_2 ($I_{\rm H2} = 15.6$ eV), thereby ensuring the importance of the C_2H_2 ionization channel. The calculated maximum electron density under base conditions (i.e. with the 4.4% CH_4/7%Ar/H_2 mixture) is $n_e \sim 3 \times 10^{11}$ cm^{-3} with $C_2H_2^+$ and $C_2H_3^+$ as the dominant ions. In the absence of hydrocarbon (e.g. a 7%Ar/H_2 mixture, under otherwise identical p and P conditions) $n_e \sim 2 \times 10^{11}$ cm^{-3} and H_3^+ is the dominant cation [65].

Under the defined base conditions, thermal-(plus plasma-) induced dissociation of molecular H_2 serves to maintain the H atom density in the center of the hot plasma ball at $\sim 4 \times 10^{16}$ cm^{-3} (equivalent to an H atom mole fraction, $X_{\rm H} \sim 8\%$). Higher $X_{\rm H}$ values can be expected in reactors operating at higher power densities. For example, $X_{\rm H}$ values of ~22% (corresponding to H atom densities $\sim 10^{17}$ cm^{-3}) are calculated [92] for the high power density (~50–120 W cm^{-3}) plasmas used in some contemporary reactors. As described previously, H atoms serve to initiate production of the various hydrocarbon radical species (e.g. CH_3) necessary for diamond growth. The model allows us to paint a coherent picture of the complex hydrocarbon inter-conversion processes occurring throughout the entire reactor volume. Figure 3 shows 2D (r, z) false-color plots depicting variation of $T_{\rm gas}$ and of the methyl radical density, [CH_3], within the Bristol MPCVD reactor operating under base conditions. Three regions are labeled in the panels of this figure: the central, hot plasma region **A**, and two hemispherical shells, **B** and **C**, characterized by different average $T_{\rm gas}$ and $X_{\rm H}$ values. As mentioned above, the CH_4 source gas is converted into C_2H_2 in region **B**, at gas temperatures 1400 K $< T_{\rm gas} <$ 2200 K, leading to local maxima of the CH_3 number density in this region. The reverse $C_2H_2 \rightarrow CH_4$ conversion dominates in region **C**, at gas temperatures 500 K $< T_{\rm gas} <$ 1400 K, with the result that C_2H_2 mole fractions shows local minima in region **C**. The identification of regions **A**–**C**, each with their own characteristic chemistries [57, 65], provides an obvious rationale for the observed insensitivity of the deposition process to the particular choice of hydrocarbon process gas (CH_4, C_2H_2, C_2H_4, C_3H_8, etc). Figure 3 also serves to illustrate the fact that the chemically reactive region (determined by the H atom activated hydrocarbon chemistry and $T_{\rm gas}$) can be considerably larger than the visible glowing plasma (associated with electron impact excitation of species that then decay radiatively) [92, 96].

The C atom, and CH, C_2 and C_2H radicals, concentrate in the hot plasma core (at $r < 2.5$ cm)—consistent with spatially resolved CH and C_2 column density measurements (and the companion model results) shown in figure 1. Conversely, the CH_4, C_2H_4, C_2H_5, C_2H_6, etc, densities all peak in the cold regions near the chamber walls [57, 65]. The overall balance lies strongly in favor of the C_2H_y group at gas temperatures 2000 K $< T_{\rm gas} <$ 3000 K, and C_2H_2 is a dominant species throughout the whole reactor volume except for the region

where the CH_4 gas source enters the reactor. The central hot region, **A**, is characterized by near-equilibrium distributions in both the C_1H_x ($x = 0$–4) and C_2H_y ($y = 0$–6) groups of species due to the rapidity of the H-shifting reactions (1), with the result that >97% of the gas phase carbon in region **A** is calculated to be in the form of C_2H_2 molecules. These facts, and the route of C_2H_y formation (reactions (2)), allows one to deduce that the CH_x and C_2H_y concentrations will approach the following dependences on input carbon mole fraction X_0 ($=X_{CH4}$ or $=2 \times X_{C2Hy}$) [65]:

$$[CH_x] \sim X_0^{0.5} \tag{3}$$

$$[C_2H_y] \sim X_0. \tag{4}$$

The square root and linear dependences on input carbon mole fraction derived in equations (3) and (4) agree, respectively, with the measured variations in CH and $C_2(a)$ column densities [61]. Dependence (3) also implies that the growth rate, G, in the case of growth from CH_3 (or any other CH_x ($x = 0$–2) species) should be proportional to the square root of the carbon fraction in the input feed gas. Such a $G(X_0)$ dependence has been reported in a number of studies [99], including the recent data of Li *et al* [100] at CH_4 input flow rates of up to a few per cent. At yet higher (>5% of the total input) flow rates, G is seen to grow more steeply, but this change is also accompanied by obvious morphological changes (from MCD to NCD) [94].

Quite apart from providing fundamental insights into the basic plasma-enhanced deposition processes, modeling can also provide useful estimates and suggest process optimization strategies. For example, the 2D model outputs together with relationship (3) provide the following practical estimate of the CH_3 mole fraction immediately proximate to the substrate and thus an upper limit estimate of G (in the framework of gas–surface kinetics [101]) for the chosen base (and similar) MPCVD reactor conditions:

$$X_{CH3} \approx 5 \times 10^{-4} X_0^{0.5} \tag{5}$$

$$G[\mu\text{m h}^{-1}] \leqslant 0.15 \times p[\text{Torr}] X_0^{0.5}. \tag{6}$$

The model outputs show that the CH_3 number density just above the substrate is 2–3 orders of magnitude higher than that of any other CH_x ($x < 3$) species and some 5 orders of magnitude higher than the C_2 number density [65], strongly suggesting that CH_3 radicals are the dominant growth species under the stated base conditions. Application of equation (6) results in maximal predicted growth rates $G \sim 4.5\ \mu\text{m h}^{-1}$ at $X_0 = 0.044$ and $p = 150$ Torr (i.e. at base reactor conditions)—a value that correlates well with the experimentally observed MCD growth rates $G \sim 2\ \mu\text{m h}^{-1}$. However, varying one reactor parameter in MPCVD growth usually affects other plasma parameters, species distributions, the gas temperature, etc, and that the detailed effect of that parameter change on growth rate is likely to be more complex than described by formula (6).

As figure 3 shows, the CH_3 number density maximizes at the periphery of the plasma region and its annular structure may introduce uniformity problems in large area depositions. Knowing the radial profiles of the H atom and CH_3 radical densities above the substrate surface allows predictions regarding the likely area of diamond deposition, uniformity and growth rates. By way of illustration, the calculated concentrations of H atoms ($\sim 1.8 \times 10^{15}$ cm^{-3}) and CH_3 radicals ($[CH_3] \sim 1.1 \times 10^{14}$ cm^{-3}) in the Bristol MPCVD reactor are near uniform across the entire top surface of the substrate (i.e. $r \leqslant 1.5$ cm), though the calculated $[CH_3]$ in this region is 3–4 times lower than the maximal CH_3 concentrations in region **B**. It may also be relevant to note that, for obvious reasons, reports of MPCVD growth of SCD generally involve small substrate areas of a few mm^2 [13, 77, 102, 103].

3. Surface chemistry

3.1. Structure

Two principal low index surfaces of the diamond crystal predominate in CVD-grown diamond materials, the C{111} and the C{100}surfaces [104–106], and while other faces have been observed macroscopically [104, 107], we shall focus our discussion on the frequently observed C{100} and the C{111} surfaces. Figure 4 displays an idealized schematic of the fully hydrogenated C{111}:H, C{110}:H, and C{100}:H 2×1 surfaces with several types of possible steps shown. The structure of the clean, hydrogen-free surfaces and the fully hydrogenated C{111} and C{100} surfaces has been reviewed numerous times [32, 108–112]. Due to the high flux of atomic hydrogen (discussed earlier) in the CVD environment, the fully hydrogenated surfaces are the most relevant to this discussion. The C{111}:H surface has a simple unreconstructed structure with a hydrogen atom terminating each surface carbon atom [112]. However, the hydrogenated C{100}:H surface is observed to have a 2×1 reconstructed surface structure with rows of surface carbons paired as dimers [113–115]. This is confirmed theoretically [111] and is due to the steric hindrance caused by the areal density of the surface carbon atoms, the need for two unpaired electrons per atom to be satisfied, and the length of the terminating CH bonds. Figure 5 shows experimental scanning tunneling microscope topographies of the C{100}:H 2×1 surface [115].

3.2. Growth mechanisms

Numerous models have been put forward over the last 20 years to explain the mechanism of carbon addition and incorporation into the diamond lattice under the CVD growth conditions. In the following discussion we shall review the current understanding of the growth mechanisms on the C{100}:H 2×1 and the C{111}:H surfaces since the Goodwin and Butler 1997 review [15].

The diamond CVD growth environment is characterized by a gaseous environment composed of molecular and atomic hydrogen (typically 1–50% H) and a dilute complex mixture of hydrocarbon molecules and radicals (<5% of the total gas phase). The concentration of electrons and ions in the high pressure thermal plasmas used for diamond CVD (in particular, MPCVD) is quite low, generally less than 10^{12} cm^{-3}

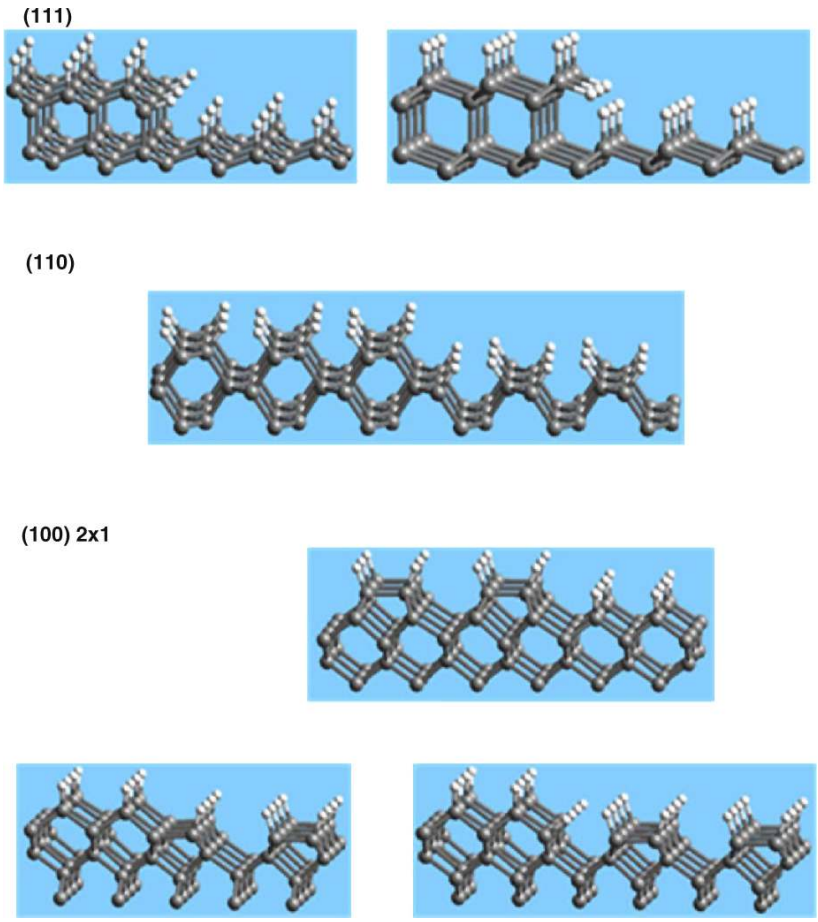

Figure 4. Idealized structures for steps on the indicated low index hydrogen-terminated diamond surfaces. The large gray balls represent carbon atoms and the small while balls represent surface bound hydrogen atoms.

(see figure 2), and shall be ignored in the following. The temperature at the growing surface is most typically between 1000 and 1200 K (occasionally 900–1600 K). The temperature of the gases may vary from near room temperature at the water-cooled walls to 2400–3700 K in the plasma or activation region. However, the temperature of the gaseous species diffusing through the thermal boundary layer and colliding with the growing surface is essentially the same as the surface temperature due to the high pressures (50–200 Torr) and short mean free paths of the gaseous species [15]. The flux of atomic hydrogen to the surface is such that each surface C atom undergoes 10^4–10^7 collisions s^{-1} with a gaseous H atom, thereby maintaining a surface terminated with CH species in steady state with a fraction of surface radicals (1–10% depending on the surface temperature) [17]. Given that the probability of the gaseous hydrogen atom abstracting a surface hydrogen to form gaseous H_2 is of the order of 0.1 per collision [116], and that the per collision probability of a surface radical recombining with an incident H atom is near unity, the surface-terminating hydrogens are rapidly exchanging with the gas and set a characteristic time or clock against which the rates of unimolecular surface reactions or rearrangements (i.e. reactions not involving a gaseous reactant) can be compared.

In the CVD growth environment, most reactions at the growing surface are either bimolecular reactions between the gaseous species and the surface site, or unimolecular migration or rearrangement reactions. Unimolecular reaction rates can be computed from the Arrhenius equation:

$$k = A \exp(-E_a/RT) \tag{7}$$

where A is the Arrhenius prefactor and E_a is the activation energy. The upper limit to the prefactor A is of the order of a vibrational period, $\sim 10^{13}$ s^{-1}, with reactions more complex than a simple bond fission having a lower value. Values of the exponential term, $(-E_a/RT)$, at a typical surface temperature of 1000 K, are given in table 1, along with the estimated upper limit on the associated reaction rates, assuming a prefactor $\leqslant 10^{13}$ s^{-1}.

The most frequent bimolecular reactions between gaseous species and the surface sites are the atomic hydrogen abstractions from the surface and atomic hydrogen recombination with the surface. In MPCVD, the flux of atomic hydrogen at the surface generally exceeds 10^{19} cm^{-2} s^{-1} and is more typically 10^{21} to 6×10^{22} cm^{-2} s^{-1}. Since the surface density of carbon atoms is 2 to 3×10^{15} cm^{-2}, each surface carbon atom experiences somewhere in the range of 10^4 to 3×10^7 gas phase H atom collisions per second. Comparing the values of the upper limits of unimolecular reaction rates, table 1, with the atomic hydrogen flux, one can see that unimolecular reactions with activation energies greater than 100–200 kJ mol^{-1} will

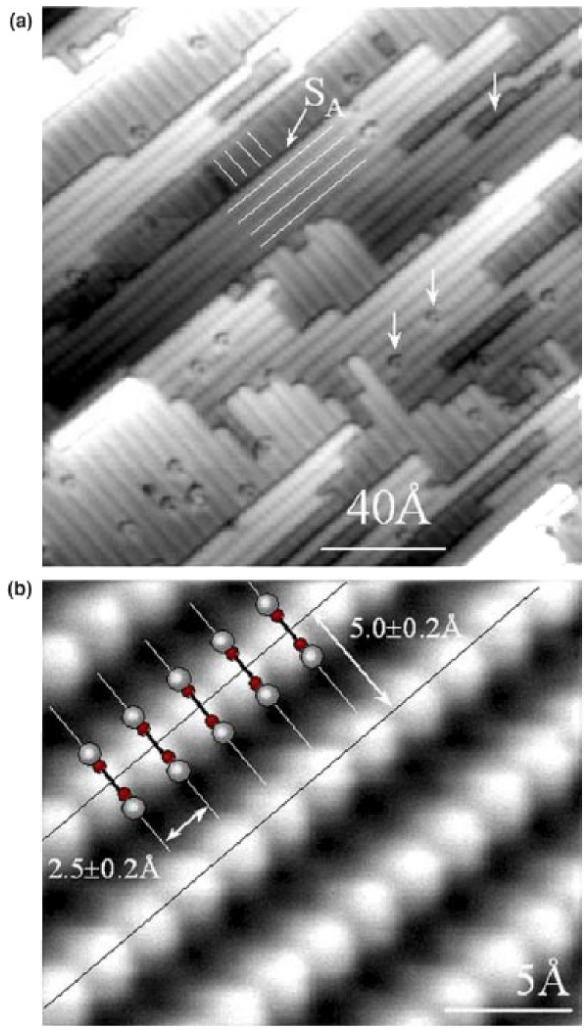

Figure 5. STM topographies of the hydrogenated diamond C{100}:H 2 × 1 surface: (a) $U_{bias} = +1.5$ V, $I_t = 1.5$ nA (unoccupied states), and (b) $U_{bias} = -1.5$ V, $I_t = 1.0$ nA (occupied states). The bright lines in the top topography indicate the C–C dimer rows in the vicinity of the step (S_a). Reprinted with permission from [115]. Copyright 2003, by the American Physical Society.

be interrupted by the atomic hydrogen bimolecular reactions at each surface site and unlikely to be important in realistic mechanisms.

Finally, the Gibbs energy is the most important quantity in determining equilibria and reaction rates. Since the surface temperatures are reasonably high, 900–1500 K in diamond CVD, entropic effects can make an important contribution to the Gibbs energy when a reaction involves the production or loss of a gas phase species. For example, a step where a gas phase methyl radical, CH_3, attaches to the surface will have an associated $\Delta_r S$ of ~ -100 J mol^{-1} K^{-1}, and the entropic contribution to the Gibbs energy at CVD growth temperatures, $T\Delta_r S$, will be $\sim$120 kJ mol^{-1}, which is sufficient to render formation of weaker C–C bonds improbable.

3.2.1. Growth on C{100}:H 2 × 1. The detailed growth mechanisms of diamond CVD on the diamond {100} surface were recently reviewed [41] and a detailed discussion based on recent computations published [117]. The following summary is derived from these two publications and publications referenced therein. The focus will be on carbon incorporation from gaseous C_1 species, e.g. CH_y ($y = 0$–3), and principally the CH_3 radical, which is strongly supported by experimental evidence [15]. The role of species containing two or more carbon atoms is restricted by their low concentration in the gas phase above the growing surface and by their short lifetime on the surface, if either adsorbed or formed on the surface, due to *beta*-scission reactions [15]. In this process, C_2H_4 and C_2H_2 molecules can be trimmed from surface-adsorbed hydrocarbon species containing two or more carbons by abstraction of a terminal hydrogen atom followed by the subsequent rearrangement to break the C–C bond *beta* to the terminal H to release the gaseous C_2H_4 or C_2H_2. At the elevated temperatures of diamond CVD, this mildly endothermic reaction occurs rapidly, as a result of the additional entropy contribution to the Gibbs energy due to the creation of the gaseous product molecule.

Table 1. The scaling of the activation energies, E_a with associated upper limits to the rates at 1000 K (in s^{-1}) assuming a prefactor, A, $\leqslant 10^{13}$ s^{-1}.

E_a (kJ mol^{-1})	$\exp(-E_a/RT)$	Rate
20	9×10^{-2}	9×10^{11}
50	2×10^{-3}	2×10^{10}
100	6×10^{-6}	6×10^{7}
200	4×10^{-11}	3×10^{2}
300	2×10^{-16}	2×10^{-3}

Carbon addition to the C{100}:H 2 × 1 dimer. The classic mechanism [118] for carbon addition to the C–H{100} 2 × 1 dimer is H abstraction of one of the dimer C–H bonds to create a surface radical, followed by the addition of a gaseous methyl radical to the surface radical site, as shown in steps **1**–**3** of figure 6. This adsorbed methyl radical is subsequently incorporated into the surface dimer bond by an additional H abstraction and bond rearrangement, steps **4**–**6** of figure 6, and the process is completed by H atom addition to the resulting surface radical, steps **6**–**7** in the figure. Table 2 reports the energetics of these steps as computed by different levels of theory [117]. The inserted CH_2 group may not be stable at the growth temperatures and potential pathways for etching/removal of the added CH_2 or CH_3 groups have been discussed [119, 120]. Such steps may be important in the generation of smooth surfaces, and these are discussed critically in [117].

An adjacent CH_2 inserted into a neighboring surface dimer along the dimer rows (the direction perpendicular to the dimer bonds) provides enough steric hindrance to alter the energetics given in figure 6 and table 2 by increasing the effective barrier to ring opening/closing and reducing the probability of CH_2 incorporation [117, 121]. However, an adjacent CH_2 group along the dimer chain, i.e. inserted across the dimer trough (discussed below), has only a minimal effect on the energetics for CH_2 incorporation into the dimer bond.

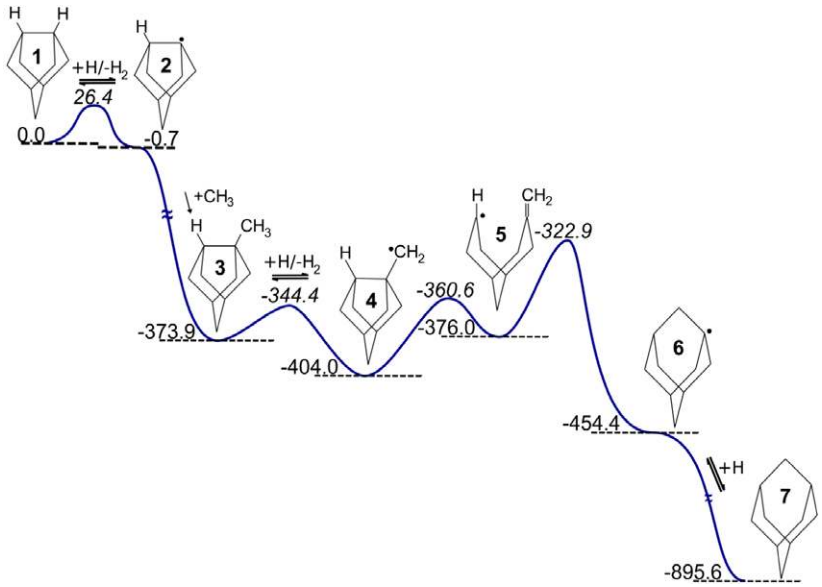

Figure 6. Reaction path for incorporating a CH_2 group into a C–C dimer bond. Energies (B3LYP QM/MM, 6-311G** basis set) are quoted in units of kJ mol^{-1}, relative to that of structure **1**. Only the atoms treated in the QM region are shown. Reprinted with permission from [117]. Copyright 2008, by the American Chemical Society.

Table 2. Energy changes, ΔE, and activation energies, E_a (both in kJ mol^{-1}), associated with the various elementary steps involved in CH_2 incorporation into the C–C dimer bond by the ring opening/closing mechanism depicted in figure 6 returned by QM/MM calculations (6-311G** basis set) and by QM calculations starting with the bare C_9H_{14} cluster, compared with previous results. References indicated in the table are from [117]. Reprinted with permission from [117]. Copyright 2008, by the American Chemical Society.

	Present study							
	QM/MM		Cluster					
Step	B3LYP	SCS-MP2	B3LYP (ref [38])	SCS-MP2	Ref [16] MRMP2	Ref [15] DFT	Refs [21, 22] PM3	Ref [13] B3LYP
$\Delta E_{1\to2}$	−0.7	25.8	−7.6	24.0	−1.7	−36.7	—	—
TS	26.4	65.7	22.9	68.7	51.0		—	28.5
$\Delta E_{2\to3}$	−373.2	−405.2	−383.7	−430.2	−372.4	−311.6	−307.9	−351.5
TS	—	—	—	—	—		—	—
$\Delta E_{3\to4}$	−30.1	−8.5	−20.1	11.5	−34.7	−79.1	—	−37.6
TS	29.5	69.1	27.6	72.3	45.2		—	25.1
$\Delta E_{4\to5}$	28.0	82.5	1.4	51.3	74.3		51.8	−2.1
TS	43.4	99.9	49.0	119.1	63.1		64.0	40.2
$\Delta E_{5\to6}$	−78.4	−124.3	−52.9	−95.8	−75.7		−100.4	−41.8
TS	53.1	58.7	58.0	77.8	50.6		51.5	59.0
$\Delta E_{4\to6}$	−50.4	−41.8	−51.5	−44.5	−1.4	−29.3	−48.6	−43.9
TS	/	/	/	/	/	54.4	/	206.7

Carbon addition across the trough in a dimer chain. Mechanisms for the incorporation of methylene, CH_2, across the trough between two adjacent dimers in the dimer chain [122, 123] are shown in figure 7 [117]. Steps **8, 9, 10, 11, 12** show methyl addition to a surface radical, followed by a second hydrogen abstraction to make a second surface radical and subsequent rearrangement to form the inserted methylene structure. Steps **8, 13, 11, 12** show a diradical pathway starting from adjacent surface radicals created by hydrogen abstraction events.

Cheesman *et al* [117] further considered three environments for CH_2 bridging the trough along the dimer chains shown in figure 8: bridging between (a) two reconstructed dimers, (b) one dimer and one with an inserted CH_2 group, and (c) both with inserted CH_2 groups. The calculated energetics for the pathways shown in figure 7 for the environments displayed in figure 8 are given in table 3. Note the increasing steric hindrance between the adsorbed methyl group and the adjacent CH bond. A conclusion of the detailed analysis of the work of Cheesman *et al* [117] is that the best site for CH_3 adsorption in the trough bridging mechanism is that shown in figure 8(b), adjacent to a dimer already bridged by a CH_2 group, i.e. on either side of a dimer already bridged by a CH_2.

Surface migration reactions. The high surface and bulk temperatures in CVD diamond growth conditions (900–

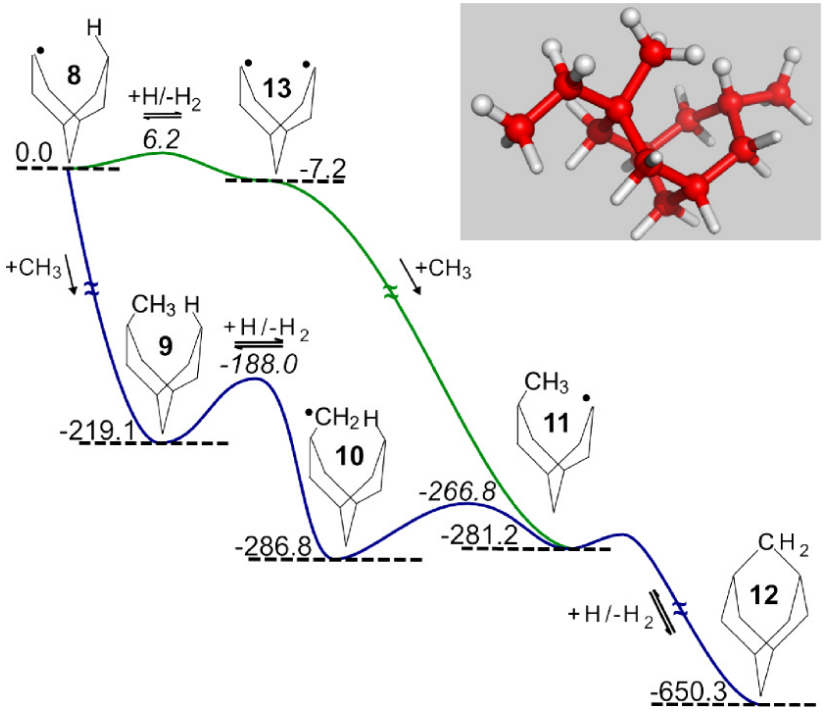

Figure 7. Reaction path(s) for incorporating a CH_2 group across the trough in a dimer chain that has one pre- and post-incorporated dimer as immediate neighbors. Energies (B3LYP QM/MM, 6-311G** basis set) are quoted in units of kJ mol^{-1}, relative to that of structure **8**. An expanded version of the QM region used for these calculations is shown in the top right-hand corner. Reprinted with permission from [117]. Copyright 2008, by the American Chemical Society.

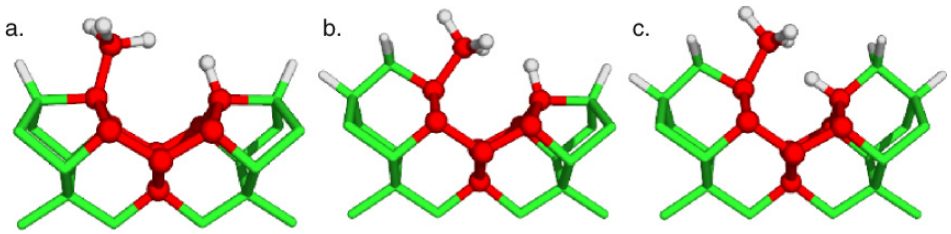

Figure 8. The three environments used when modeling the dimer trough bridging mechanism for carbon incorporation on a 2 × 1 reconstructed, H-terminated diamond (100) surface: (a) nucleation; (b) propagation; (c) termination step. The displayed structures correspond to three variants of structure **9** in figure 3, with the QM region highlighted in red. Reprinted with permission from [117]. Copyright 2008, by the American Chemical Society.

1500 K) are sufficient to desorb even strongly bound species such as carbon adsorbates and even hydrogen [124, 125]. Hence, it would seem unlikely that adsorbates would diffuse across the surface as opposed to desorb back to the gas phase. However, the surfaces observed after CVD growth are often reasonably smooth. The random addition of single carbon species to the C{100} surface should not result in smooth surfaces. This is further observed in the mesoscale modeling discussed later. Surface migration of certain species might explain this. This topic has been examined and discussed by Frenklach and Skokov [126] and more recently by Cheesman *et al* [117].

On the pristine C{100}:H 2 × 1 surface migration of a radical site is the same as the migration of a hydrogen atom and is calculated to have large (>300 kJ mol^{-1}) activation barriers [117]. However, hopping of the radical site between the surface dimer and an adjacent adsorbed CH_3 group was found to be feasible, e.g. steps **10–11** in figure 7.

Migration of carbon species, e.g. CH_2 and C=CH_2, is feasible when biradical sites are formed. Figure 9 displays the energetics calculated for a CH_2 group migrating along the dimer chain, while figure 10 displays a path for migration along the dimer rows [117]. The maximum calculated energy barriers—145.5 kJ mol^{-1} (figure 9), 111.3 kJ mol^{-1} (figure 10)—suggest that these processes will occur on a timescale (see table 1) similar to the rate of gaseous H atoms terminating the radical sites and stopping any such hopping. Potential energy surfaces (PES) involving biradicals form spin triplet and singlet states, and the crossing of, and inter-conversion between, these is discussed in more detail in [117].

Dimer generation. A detailed mechanism for the formation of a new surface dimer on the next layer in the direction of growth has been proposed by Cheesman *et al* [117]. It begins with an already inserted CH_2 group on a lower layer dimer and, through hydrogen abstraction, methyl addition at

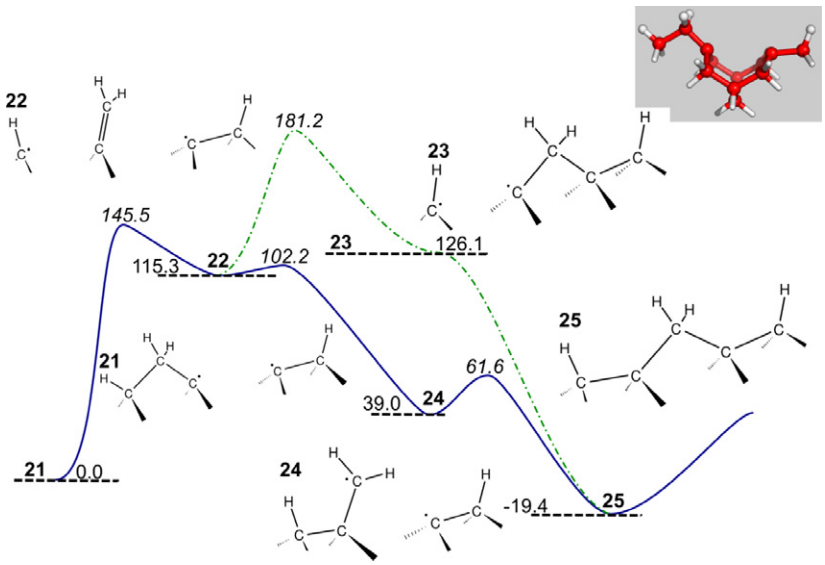

Figure 9. PES describing migration of a CH_2 group along a dimer chain on the 2 × 1 reconstructed, H-terminated diamond (100) surface. Optimized structures of the intermediates returned by the QM/MM calculations are shown, with the QM region used in these calculations shown in the top right-hand corner. Energies (B3LYP QM/MM, 6-311G** basis set) are quoted in units of kJ mol^{-1}, relative to that of structure **21**. Reprinted with permission from [117]. Copyright 2008, by the American Chemical Society.

Table 3. Calculated (QM/MM, 6-311G** basis set) energy changes, ΔE, and activation energies, E_a, (both in kJ mol^{-1}) associated with the various elementary steps involved in CH_2 incorporation across the trough between successive dimers in a chain as depicted in figure 7 for three local variants of **9** with small QM regions as defined in figure 8 and the larger QM region in the case of the one neighboring inclusion as shown in figure 7. References indicated in the table are from [117]. Reprinted with permission from [117]. Copyright 2008, by the American Chemical Society.

	Pristine surface		1 neighboring inclusion			2 neighboring inclusions	
	(–·–)		(∧.–)			(∧.∧)	
	(Figure 8(a))		(Figure 8(b))			(Figure 8(c))	
	Small QM	PM3 (ref [22])	Small QM	Large QM	PM3 (ref [22])	Small QM	PM3 (ref [22])
Steric route							
8 → **9**	−389.7	−312.5	−245.6	−219.1	−101.3	−149.3	45.6
TS		0.0		0.0	61.9		101.3
9 → **10**	−21.1	43.5	−67.9	−67.7		−114.4	
TS				31.1			
10 → **11**	8.5	43.5	6.3	5.7		−12.5	
TS		81.2		20.0			
Diradical							
8 → **13**	4.1		5.2	−7.2		−5.1	
TS				6.2			
13 → **11**	−406.4	−315.5	−312.5	−274.0	−195.8	−271.1	−129.3
TS		0.0		0.0	10.0		36.0
Ring closing							
11 → **12**	−113.1		−377.3	−369.1		−516.7	

the CH_2 group, followed by further hydrogen abstractions and rearrangements, bridges two adjacent lower layer (previously) dimers to form a new dimer on the new layer rotated by 90° as shown in figure 11. This mechanism (and variations on it) have been discussed in detail [117] and, for conciseness, is not repeated here.

In the preceding discussion, plausible mechanisms have been demonstrated for the carbon inclusion in the C{100}:H 2 × 1 surface dimers, the bridging of the troughs between dimers along the dimer chains, and hopping migration of CH_2 groups along both dimer chains and rows. Migration of H atoms (surface radicals) only appears feasible in exceptional cases, e.g. steps **10**–**11** in figure 7. Finally, a mechanism for the formation of new surface dimers on the next layer of growth has been proposed by Cheesman *et al* [117].

3.2.2. Growth on C{111}:H. Growth on a C{111}:H surface has not been well addressed in the literature, and especially not to the level of computational theory that has been used for C{100}:H 2 × 1 surfaces. Aside from the mesoscale modeling studies addressed in the next section, one recent paper discusses growth on the C{111}:H surface [46]. The

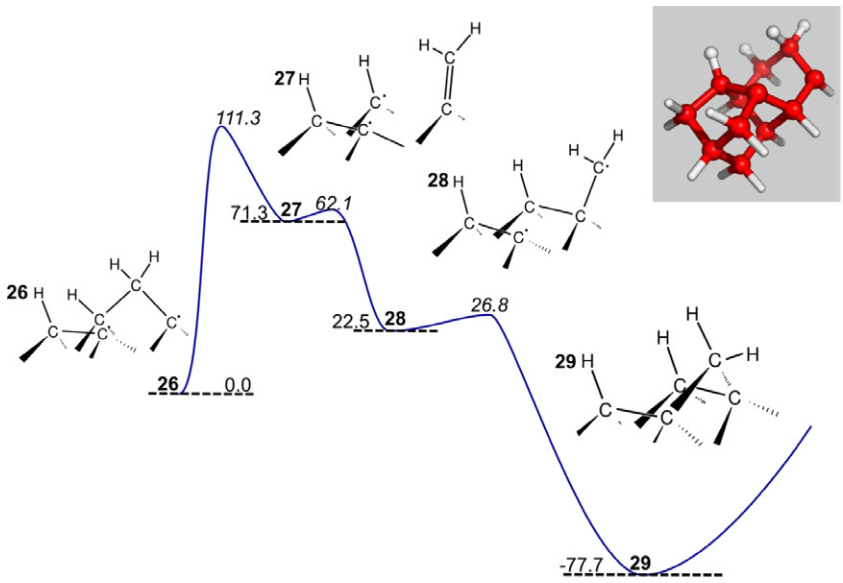

Figure 10. PES describing migration of a CH_2 group on the 2×1 reconstructed, H-terminated diamond (100) surface. Optimized structures of the intermediates returned by the QM/MM calculations are shown, with the QM region used in these calculations shown in the top right-hand corner. Energies (B3LYP QM/MM, 6-311G** basis set) are quoted in units of kJ mol^{-1}, relative to that of structure **26**. Reprinted with permission from [117]. Copyright 2008, by the American Chemical Society.

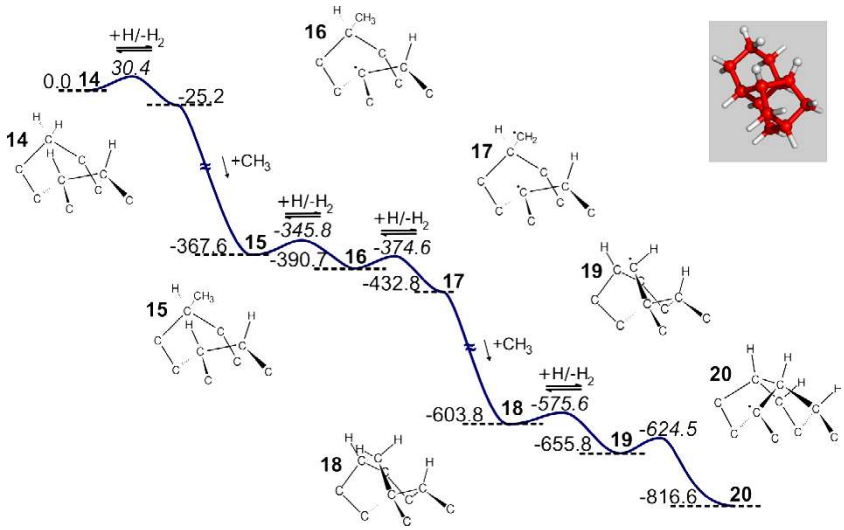

Figure 11. PES illustrating the way in which CH_3 radical addition can lead to nucleation of a new reconstructed dimer layer on the diamond {100} surface. Optimized structures of the intermediates returned by the QM/MM calculations are illustrated, with the QM region used in these calculations shown in the top right-hand corner. Energies (B3LYP QM/MM, 6-311G** basis set) are quoted in units of kJ mol^{-1}, relative to that of structure **14**. Reprinted with permission from [117]. Copyright 2008, by the American Chemical Society.

main point of this work is that growth on the C{111}:H surface is limited by the rate of formation of a critical four-atom nucleus on the surface. Once this 'nucleus' of the next layer is formed, it can grow rapidly at its edges by one-and two-carbon growth processes. The model predicts several interesting consequences. First, the four-atom 'nucleus' for next layer growth has a 50:50 chance of forming a stacking fault (a contact twin). Second, the rate of formation of the four-atom 'nucleus' can be significantly enhanced by the addition of two-atom surface species, e.g. CN, which are insensitive to the *beta*-scission process that otherwise limits the probability of finding two-(non-hydrogen) atom adsorbate species. This latter process can significantly enhance the growth rate on {111} surfaces.

4. Growth modeling

Mesoscale modeling of the growth of a macroscopic block of diamond involves a large number of gas phase species and surface reactions. Kinetic Monte Carlo (KMC) protocols have been explored to model the growth of diamond. In the KMC process, each reaction increment is randomly selected using a time-based probability algorithm from all the possible reactions. For each step, a complete table of the possible events

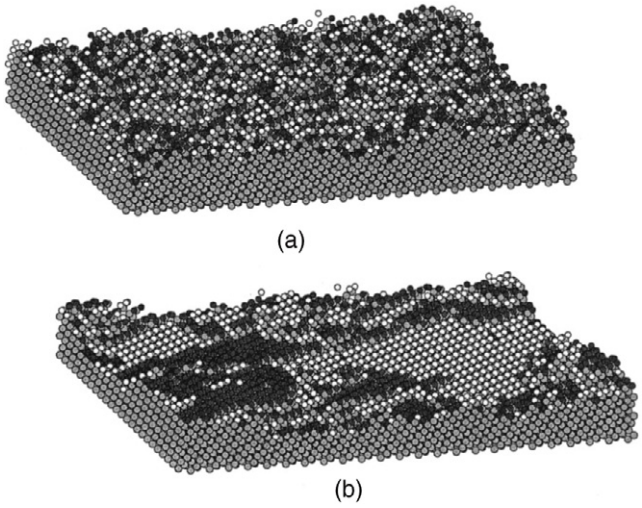

Figure 12. Images of {100} films during simulated growth at 1200 K (a) without and (b) with etching. Light gray atoms are carbons in the diamond film. The hydrogen atoms are shaded according to their height. Two gray levels (dark gray and white) are used and cycle every two layers. Reprinted with permission from [120]. Copyright 1997, by the American Institute of Physics.

at a given temperature is prepared and the simulation then randomly chooses an event (as weighted by the relative rates) and advances the timeclock by a characteristic time (see [127] for more details). The weaknesses of the KMC approach are: (1) the results can be readily distorted by missing or erroneous processes; (2) the process does not offer direct insight into new mechanisms; and (3) the results generated can only be validated by suitable experimental data.

Early kinetic investigations of diamond growth looked at the direct incorporation of incident carbon species using simple adsorption models for carbon species [83, 128]. These models reproduced available experimental growth rates fairly well, but offered little insight into the surface chemistry. The shortcomings of these initial models led to an expansion of the modeling to include more complex reaction dynamics like surface migrations [129] and etching of surface atoms [130].

Battaile *et al* [119, 120, 131–134] used KMC modeling based upon previously reported energetics in the literature and considered diamond growth occurring by methyl radicals via the trough bridging incorporation mechanism (discussed in conjunction with the incorporation of acetylene). These studies highlighted the importance of substrate orientations and the roles of C_2H_2 in controlling the growth rate. While this model predicted the growth rates observed on {111} and {110} surfaces reasonably well, the results for {100} predicted neither the experimental growth rate nor the smooth facets observed in growth. However, the inclusion of a step etching of the carbon adsorbate within the KMC calculations, CH_3 dissociation from the surface (calculated at the PM3 theory level), allowed the production of large and smooth terraces on the {100} diamond surface (see figure 12) and gave reasonable agreement with the experimental growth rates [130]. This KMC work also indirectly highlighted the effects that 'new-layer nucleation' can have upon the growth rate and growing crystal morphology [131]. Modeling of 'off-axis' growth on the {111} face predicted structures comparable with 'step-flow' growth resulting from a faster rate for lateral growth versus new-layer nucleation [119]. This effect is highly surface-specific as misalignment upon the {100} face had minimal effect upon the morphology.

Grujicic and Lai have used an expanded KMC protocol to model a hot filament CVD growth reactor by directly coupling a gas phase reactor model to provide the calculated number densities for various surface sites on both the {111} [135] and {100} [136] surfaces. The resulting surfaces are shown in figures 13 and 14, respectively. Despite the identical gas phase and gas–surface chemistry used in both scenarios, the {111} model produces a rough surface showing a higher concentration of defects, including twinning, kinks and vacancies. The model has large smooth terraces, attributed to the poor rate of nucleation of the next layer of growth (see also [46]). The {100} surface, however, is rough on the atomic scale, shows no long range structure or defects and is lacking the dimer reconstructions.

The most recent and extensive implementation of KMC modeling of diamond growth is by Frenklach *et al* [129]. It

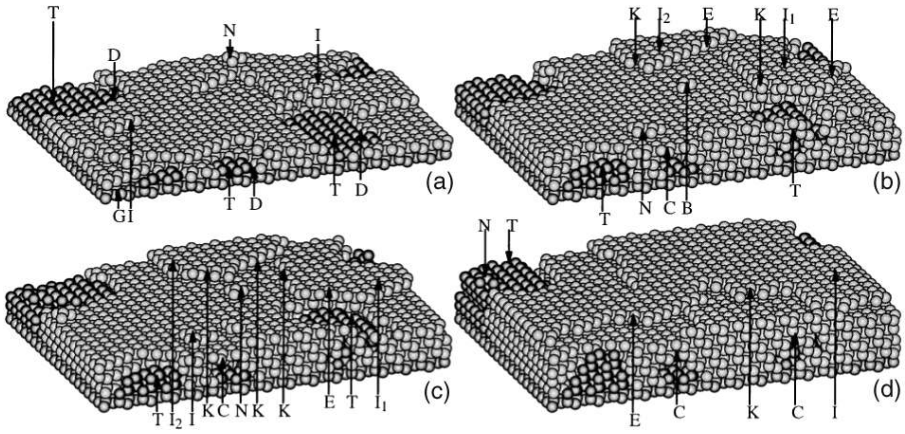

Figure 13. Top view of a (111)-oriented diamond film simulated under the following CVD conditions in the reactor: reactive gas at the reactor inlet (0.4% CH_4, 92.5% H_2), $T_{heator} = 2000$ K, $T_{substrate} = 1000$ K, $p = 20.25$ Torr, Heater-to-substrate distance = 1.3 cm. Deposition times: (a) 0.87 s; (b) 1.81 s; (c) 2.07 s and (d) 2.85 s. Nomenclature: B—three-carbon bridge, C—twin covered by regular crystal, D—dislocation loop, E—edge, G—gap, I—island, K—kink, N—nucleus, T—twin, V—void. Reprinted with permission from [136]. Copyright 2000, by Springer.

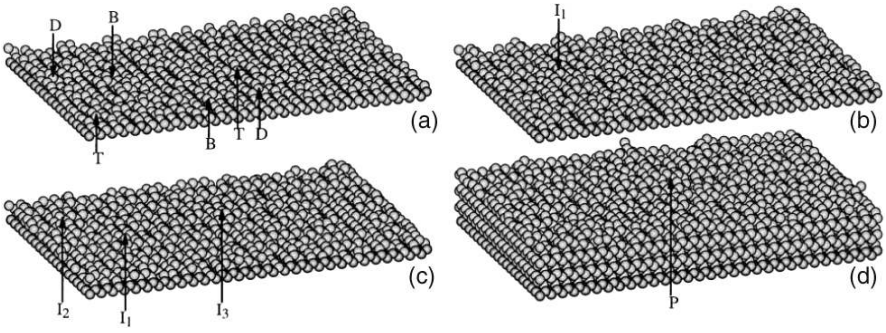

Figure 14. Top view of four {100} surface configurations obtained under the CVD conditions identical to the ones listed in figure 13. Deposition times: (a) 0.01 s; (b) 0.018 s; (c) 0.032 s and (d) 0.208 s. Nomenclature: B—BCN mechanism (i.e. CH_3 insertion across a trough by the HH mechanism), D—dimer insertion mechanism, P—pit, I—island, T—trough. Reprinted with permission from [136]. Copyright 2000, by Springer.

assumed CH_3 radicals as the sole growth species and describes carbon incorporation into the diamond surface by means of the ring opening/closing mechanism. CH_2 migration along and across the dimer reconstructions was included, as well as the reforming of the surface reconstruction bonds from two suitable adjacent surface radical sites. Etching was only considered to occur at isolated incorporated CH_2 groups and reconstructed dimers. Etching the former is described by the removal of CH_2 with the reverse of the ring opening/closing incorporation mechanism and the removal of isolated dimer reconstructions by a one-or two-carbon removal process. The energetics and kinetic data for these reactions are derived from numerous calculations and experimental measurements in hydrocarbon chemistry. The initial model failed to produce continuous rows of incorporated CH_2 species (similar to that obtained in [137]), but the subsequent reports [129] include a compensatory term to ensure saturation of these sites. The latter is parameterized through optimization of the growth rate [129].

The Frenklach KMC work [129] highlights the positive effect that surface migration has upon the diamond growth rates, where an ∼1 order of magnitude enhancement of growth rate is predicted compared to that for adsorption-only growth. This KMC study explored the effects of varying numerous process conditions, including the abundance of reagents and substrate temperature [129]. The resultant films 'grown' under these KMC conditions show wide variations in surface roughness, with the formation of {111} domains, most unlike the pristine starting diamond surface. The results do not show smooth terrace growth of diamond and suggest that the growth process is similar to island-type growth. However, upon closer examination of the mechanisms proposed, there is no direct mechanism for forming the dimer reconstructions. Instead, dimer formation is suggested to occur as a by-product of migration of incorporated CH_2, or via the coalescence of two neighboring carbon surface radicals.

The Frenklach growth model [129] also shows that, without the growth species present, the etching reactions on the rough {100} diamond surface can produce the experimentally observed smooth surfaces. The necessary time frame for this process might be short enough for it to occur during the process of shutting down a reactor. However, the model lacks feasible etching processes for CH_x species, as the only process included is the expulsion of CH_3 by the fission of a strong C–C surface bond (there is no provision for a *beta*-scission etching reaction). The Frenklach model suggests that carbon, in the form of CH_3, can randomly incorporate upon a diamond {100} surface and undergo migration across the surface until multiple species coalesce. During this process, the substrate surface can act as a template for migrating species to form new dimer reconstructions and, in combination with etching (especially under post-growth conditions), could result in the smooth surface growth observed [138]. As discussed earlier, this migration depends on the formation of adjacent surface radical sites and can be disrupted by the adsorption of gaseous H atoms.

5. Summary

Our understanding of diamond chemical vapor deposition has progressed greatly since the early work of the 1980s and 1990s. More sophisticated and detailed *in situ* diagnostics of the growth environment, particularly of the MPCVD reactors, assisted by the development of 2D models of the chemical and plasma processes and gas dynamics, have provided insights into the complex processes that provide the reactive species to the growing diamond surfaces. The complex reactions on the growing diamond surfaces are now understood in much better detail, particularly for the C(100):H 2×1 surface, as a result of insights developed from different levels of computational calculations. Full understanding of the complex environment in which diamond CVD occurs will require further integration of sophisticated experimental measurements, advanced modeling of the detailed surface chemistry and of gas mixture activation processes, and their extension to reactor scale engineering.

Acknowledgments

JEB acknowledges the support of ONR/NRL. The Bristol group is grateful to: EPSRC for the award of a portfolio grant (LASER); Element Six Ltd for financial support and the long term loan of the MW reactor; University of Bristol and the Overseas Research Scholarship (ORS) scheme for a postgraduate scholarship (JM); and to colleagues K N Rosser,

Drs J A Smith and C M Western, and Professor A J Orr-Ewing for their many contributions to the work described here. YuAM acknowledges support from the RF Government for Key Science Schools grant no. 133.2008.2. The Bristol–Moscow collaboration is supported by a Royal Society Joint Project Grant.

References

[1] Angus J C and Hayman C C 1988 Low-pressure, metastable growth of diamond and diamondlike phases *Science* **241** 913–21

[2] Yarbrough W A and Messier R 1990 Current issues and problems in the chemical vapor-deposition of diamond *Science* **247** 688–96

[3] Butler J E and Windischmann H 1998 Developments in CVD-diamond synthesis during the past decade *MRS Bull.* **23** 22–7

[4] May P W 2000 Diamond thin films: a 21st-century material *Phil. Trans. R. Soc.* A **358** 473–95

[5] Gruen D M, Pan X Z, Krauss A R, Liu S Z, Luo J S and Foster C M 1994 Deposition and characterization of nanocrystalline diamond films *J. Vac. Sci. Technol.* A **12** 1491–5

[6] Gruen D M 1999 Nanocrystalline diamond films *Annu. Rev. Mater. Sci.* **29** 211–59

[7] Butler J E and Sumant A V 2008 The CVD of nanodiamond materials *Chem. Vapor Depos.* **14** 145–60

[8] Ong T P and Chang R P H 1989 Low-temperature deposition of diamond films for optical coatings *Appl. Phys. Lett.* **55** 2063–5

[9] Windischmann H and Epps G F 1990 Properties of diamond membranes for x-ray-lithography *J. Appl. Phys.* **68** 5665–73

[10] Gray K J and Windischmann H 1999 Free-standing CVD diamond wafers for thermal management by d.c. arc jet technology *Diamond Relat. Mater.* **8** 903–8

[11] www.e6cvd.com

[12] Wang W Y, Moses T, Linares R C, Shigley J E, Hall M and Butler J E 2003 Gem-quality synthetic diamonds grown by a chemical vapor deposition (CVD) method *Gems Gemol.* **39** 268–83

[13] Yan C S, Vohra Y K, Mao H K and Hemley R J 2002 Very high growth rate chemical vapor deposition of single-crystal diamond *Proc. Natl Acad. Sci. USA* **99** 12523–5

[14] Bogdan G, De Corte K, Deferme W, Haenen K and Nesladek M 2006 Thick single crystal CVD diamond prepared from CH_4-rich mixtures *Phys. Status Solidi* a **203** 3063–9

[15] Goodwin D G and Butler J E 1997 Theory of diamond chemical vapor deposition *Handbook of Industrial Diamonds and Diamond Films* ed M A Prelas *et al* (New York: Dekker) pp 527–81

[16] Angus J C, Argoitia A, Gat R, Li Z, Sunkara M, Wang L and Wang Y 1993 Chemical vapor-deposition of diamond *Phil. Trans. R. Soc.* A **342** 195–208

[17] Butler J E and Woodin R L 1993 Thin-film diamond growth mechanisms *Phil. Trans. R. Soc.* A **342** 209–24

[18] Celii F G, Pehrsson P E, Wang H T and Butler J E 1988 Infrared detection of gaseous species during the filament-assisted growth of diamond *Appl. Phys. Lett.* **52** 2043–5

[19] Celii F G and Butler J E 1989 Hydrogen-atom detection in the filament-assisted diamond deposition environment *Appl. Phys. Lett.* **54** 1031–3

[20] Harris S J, Weiner A M and Perry T A 1988 Measurement of stable species present during filament-assisted diamond growth *Appl. Phys. Lett.* **53** 1605–7

[21] Harris S J, Weiner A M and Perry T A 1991 Filament-assisted diamond growth-kinetics *J. Appl. Phys.* **70** 1385–91

[22] Harris S J and Weiner A M 1992 Diamond growth-rates versus acetylene concentrations *Thin Solid Films* **212** 201–5

[23] Wu C H, Tamor M A, Potter T J and Kaiser E W 1990 A study of gas chemistry during hot-filament vapor-deposition of diamond films using methane hydrogen and acetylene hydrogen gas-mixtures *J. Appl. Phys.* **68** 4825–9

[24] Chu C J, D'Evelyn M P, Hauge R H and Margrave J L 1990 Mechanism of diamond film growth by hot-filament CVD ^{13}C studies *J. Mater. Res.* **5** 2405–13

[25] Goodwin D G and Gavillet G G 1990 Numerical modeling of the filament-assisted diamond growth environment *J. Appl. Phys.* **68** 6393–400

[26] Schafer L, Klages C P, Meier U and Kohsehoinghaus K 1991 Atomic-hydrogen concentration profiles at filaments used for chemical vapor-deposition of diamond *Appl. Phys. Lett.* **58** 571–3

[27] Celii F G and Butler J E 1992 Direct monitoring of CH_3 in a filament-assisted diamond chemical vapor-deposition reactor *J. Appl. Phys.* **71** 2877–83

[28] Gat R and Angus J C 1993 Hydrogen-atom recombination on tungsten and diamond in hot-filament assisted deposition of diamond *J. Appl. Phys.* **74** 5981–9

[29] McMaster M C, Hsu W L, Coltrin M E and Dandy D S 1994 Experimental measurements and numerical simulations of the gas-composition in a hot-filament-assisted diamond chemical-vapor-deposition reactor *J. Appl. Phys.* **76** 7567–77

[30] Smith J A, Cameron E, Ashfold M N R, Mankelevich Y A and Suetin N V 2001 On the mechanism of CH_3 radical formation in hot filament activated CH_4/H_2 and C_2H_2/H_2 gas mixtures *Diamond Relat. Mater.* **10** 358–63

[31] Mankelevich Y A, Suetin N V, Ashfold M N R, Smith J A and Cameron E 2001 Experimental data versus 3-d model calculations of HFCVD processes: correlations and discrepancies *Diamond Relat. Mater.* **10** 364–9

[32] Celii F G and Butler J E 1991 Diamond chemical vapor-deposition *Annu. Rev. Phys. Chem.* **42** 643–84

[33] Thorsheim H R and Butler J E 1994 *Synthetic Diamond: Emerging CVD Science and Technology* ed K Spear and J Dismukes (New York: Wiley-Interscience) pp 193–242

[34] Railkar T A, Kang W P, Windischmann H, Malshe A P, Naseem H A, Davidson J L and Brown W D 2000 A critical review of chemical vapor-deposited (CVD) diamond for electronic applications *Crit. Rev. Solid State Mater. Sci.* **25** 163–277

[35] Varnin V P, Laptev V A and Ralchenko V G 2006 The state of the art in the growth of diamond crystals and films *Inorg. Mater.* **42** S1–18

[36] Das D and Singh R N 2007 A review of nucleation, growth and low temperature synthesis of diamond thin films *Int. Mater. Rev.* **52** 29–64

[37] Man W D, Wang J H, Wang C X and Ma Z B 2002 The properties, production and applications of diamond thin films *New Carbon Mater.* **17** 62–70

[38] Marinkovic S N 2004 *Chemistry and Physics of Carbon* (New York: Dekker) pp 71–207

[39] Williams O A and Nesladek M 2006 Growth and properties of nanocrystalline diamond films *Phys. Status Solidi* a **203** 3375–86

[40] Ashfold M N R, May P W, Petherbridge J R, Rosser K N, Smith J A, Mankelevich Y A and Suetin N V 2001 Unravelling aspects of the gas phase chemistry involved in diamond chemical vapour deposition *Phys. Chem. Chem. Phys.* **3** 3471–85

[41] Butler J E, Cheesman A and Ashfold M N R 2009 *CVD Diamond for Electronic Devices and Sensors* ed R S Sussmann (Chichester: Wiley) pp 103–24

[42] Sunkara M, Angus J C, Hayman C C and Buck F A 1990 Nucleation of diamond crystals *Carbon* **28** 745–6

[43] Pehrsson P E, Celii F G and Butler J E 1993 *Diamond Films and Coatings* ed R Davis (Park Ridge, NJ: Noyes Publications) pp 68–146

[44] Liu H and Dandy D S 1995 *Diamond Chemical Vapor Deposition—Nucleation and Early Growth Stages* (Park Ridge, NJ: Noyes Publications)

[45] Bachmann P K, Leers D and Lydtin H 1991 Towards a general concept of diamond chemical vapour deposition *Diamond Relat. Mater.* **1** 1–12

[46] Butler J E and Oleynik I 2008 A mechanism for crystal twinning in the growth of diamond by chemical vapour deposition *Phil. Trans. R. Soc.* A **366** 295–310

[47] Wu J J and Hong F C N 1997 Effect of chlorine addition on diamond growth using methane/hydrogen reactants *J. Appl. Phys.* **81** 3647–51

[48] Hirose Y and Kondo N 1988 *Program and Book of Abstracts, Japanese Applied Physics 1988 Spring Mtg (March 1988)*

[49] Matsui Y, Yuuki A, Sahara M and Hirose Y 1989 Flame structure and diamond growth-mechanism of acetylene torch *Japan. J. Appl. Phys.* 1 **28** 1718–24

[50] Carrington W A, Hanssen L M, Snail K A, Oakes D B and Butler J E 1989 Diamond growth in $O_2 + C_2H_4$ and $O_2 + C_2H_2$ flames *Metall. Trans.* A **20** 1282–4

[51] Lombardi G, Hassouni K, Stancu G D, Mechold L, Ropcke J and Gicquel A 2005 Study of an H_2/CH_4 moderate pressure microwave plasma used for diamond deposition: modelling and IR tuneable diode laser diagnostic *Plasma Sources Sci. Technol.* **14** 440–50

[52] Lombardi G, Stancu G D, Hempel F, Gicquel A and Ropcke J 2004 Quantitative detection of methyl radicals in non-equilibrium plasmas: a comparative study *Plasma Sources Sci. Technol.* **13** 27–38

[53] Lombardi G, Hassouni K, Benedic F, Mohasseb F, Ropcke J and Gicquel A 2004 Spectroscopic diagnostics and modeling of $Ar/H_2/CH_4$ microwave discharges used for nanocrystalline diamond deposition *J. Appl. Phys.* **96** 6739–51

[54] Butler J E, Celii F G, Oakes D B, Hanssen L M, Carrington W A and Snail K A 1989 Studies of diamond chemical vapor-deposition *High Temp. Sci.* **27** 183–97

[55] Hirmke J, Glaser A, Hempel F, Stancu G D, Ropcke J, Rosiwal S M and Singer R F 2007 Improved flow conditions in diamond hot filament CVD—promising deposition results and gas phase characterization by laser absorption spectroscopy *Vacuum* **81** 619–26

[56] Cheesman A, Smith J A, Ashfold M N R, Langford N, Wright S and Duxbury G 2006 Application of a quantum cascade laser for time-resolved, *in situ* probing of CH_4/H_2 and C_2H_2/H_2 gas mixtures during microwave plasma enhanced chemical vapor deposition of diamond *J. Phys. Chem.* A **110** 2821–8

[57] Ma J, Cheesman A, Ashfold M N R, Langford N, Wright S, Duxbury G and Mankelevich Y A 2009 Quantum cascade laser investigations of CH_4 and C_2H_2 inter-conversion in hydrocarbon/H_2 gas mixtures during microwave plasma enhanced chemical vapor deposition of diamond *J. Appl. Phys.* at press

[58] Cappelli M A, Owano T G, Gicquel A and Duten X 2000 Methyl concentration measurements during microwave plasma-assisted diamond deposition *Plasma Chem. Plasma Proc.* **20** 1–12

[59] John P, Rabeau J R and Wilson J I B 2002 The cavity ring-down spectroscopy of C_2 in a microwave plasma *Diamond Relat. Mater.* **11** 608–11

[60] Rabeau J R, John P, Wilson J I B and Fan Y 2004 The role of C_2 in nanocrystalline diamond growth *J. Appl. Phys.* **96** 6724–32

[61] Ma J, Richley J C, Ashfold M N R and Mankelevich Y A 2008 Probing the plasma chemistry in a microwave reactor used for diamond chemical vapor deposition by cavity ring down spectroscopy *J. Appl. Phys.* **104** 103305

[62] Wheeler M D, Newman S M, Orr-Ewing A J and Ashfold M N R 1998 Cavity ring-down spectroscopy *J. Chem. Soc. Faraday Trans.* **94** 337–51

[63] Rothman L S, Barbe A, Benner D C, Brown L R, Camy-Peyret C, Carleer M R, Chance K, Clerbaux C, Dana V, Devi V M, Fayt A, Flaud J M, Gamache R R, Goldman A, Jacquemart D, Jucks K W, Lafferty W J, Mandin J Y, Massie S T, Nemtchinov V, Newnham D A, Perrin A, Rinsland C P, Schroeder J, Smith K M, Smith M A H, Tang K, Toth R A, Vander Auwera J, Varanasi P and Yoshino K 2003 The HITRAN molecular spectroscopic database: edition of 2000 including updates through 2001 *J. Quant. Spectrosc. Radiat. Transfer* **82** 5–44

[64] Hassouni K, Lombardi G, Duten X, Haagelar G, Silva F, Gicquel A, Grotjohn T A, Capitelli M and Ropcke J 2006 Overview of the different aspects in modelling moderate pressure H_2 and H_2/CH_4 microwave discharges *Plasma Sources Sci. Technol.* **15** 117–25

[65] Mankelevich Y A, Ashfold M N R and Ma J 2008 Plasma-chemical processes in microwave plasma-enhanced chemical vapor deposition reactors operating with C/H/Ar gas mixtures *J. Appl. Phys.* **104** 113304

[66] Zhu W, Inspektor A, Badzian A R, McKenna T and Messier R 1990 Effects of noble-gases on diamond deposition from methane-hydrogen microwave plasmas *J. Appl. Phys.* **68** 1489–96

[67] Gicquel A, Hassouni K, Farhat S, Breton Y, Scott C D, Lefebvre M and Pealat M 1994 Spectroscopic analysis and chemical kinetics modeling of a diamond deposition plasma reactor *Diamond Relat. Mater.* **3** 581–6

[68] Gicquel A, Chenevier M, Breton Y, Petiau M, Booth J P and Hassouni K 1996 Ground state and excited state H-atom temperatures in a microwave plasma diamond deposition reactor *J. Physique* **6** 1167–80

[69] Gicquel A, Hassouni K, Breton Y, Chenevier M and Cubertafon J C 1996 Gas temperature measurements by laser spectroscopic techniques and by optical emission spectroscopy *Diamond Relat. Mater.* **5** 366–72

[70] Gicquel A, Chenevier M, Hassouni K, Tserepi A and Dubus M 1998 Validation of actinometry for estimating relative hydrogen atom densities and electron energy evolution in plasma assisted diamond deposition reactors *J. Appl. Phys.* **83** 7504–21

[71] Lang T, Stiegler J, vonKaenel Y and Blank E 1996 Optical emission diagnostics and film growth during microwave-plasma-assisted diamond CVD *Diamond Relat. Mater.* **5** 1171–84

[72] Goyette A N, Lawler J E, Anderson L W, Gruen D M, McCauley T G, Zhou D and Krauss A R 1998 Swan band emission intensity as a function of density *Plasma Sources Sci. Technol.* **7** 149–53

[73] Rousseau A, Granier A, Gousset G and Leprince P 1994 Microwave-discharge in H_2—influence of H-atom density on the power balance *J. Phys. D: Appl. Phys.* **27** 1412–22

[74] Geng Z C, Xu Y, Yang X F, Wang W G and Zhu A M 2005 Atomic hydrogen determination in medium-pressure microwave discharge hydrogen plasmas via emission actinometry *Plasma Sources Sci. Technol.* **14** 76–82

[75] Gicquel A, Chenevier M and Lefebvre M 1997 Spatially resolved spectroscopic analysis of the plasma *Handbook of Industrial Diamonds and Diamond Films* ed M A Prelas *et al* (New York: Dekker) pp 739–96

[76] Ma J, Ashfold M N R and Mankelevich Y A 2009 Validating optical emission spectroscopy as a diagnostic of microwave activated $CH_4/Ar/H_2$ plasmas used for diamond chemical vapor deposition *J. Appl. Phys.* **105** 043302

[77] Liang Q, Chin C Y, Lai J, Yan C S, Meng Y, Mao H K and Hemley R J 2009 Enhanced growth of high quality single crystal diamond by microwave plasma assisted chemical vapor deposition at high gas pressures *Appl. Phys. Lett.* **94** 024103

[78] Rayar M, Veis P, Foissac C, Supiot P and Gicquel A 2006 Gas temperature determination using BH (0–0) $A\,^1\Pi \rightarrow X\,^1\sum^+$ emission spectrum in a B_2H_6 containing plasma for doped diamond deposition *J. Phys. D: Appl. Phys.* **39** 2151–9

[79] Ma J, Richley J C, Davies D R W, Ashfold M N R and Mankelevich Y A 2009 Spectroscopic and modeling investigations of the gas phase chemistry and composition in microwave plasma activated $B_2H_6/CH_4/Ar/H_2$ mixtures, in preparation

[80] Olivas-Martinez M, Perez-Tello M, Cabanillas-Lopez R, Contreras-Lopez O, Soto-Herrera G and Castillon-Barraza F 2007 A computational model for the hot-filament chemical vapour deposition process to produce diamond films *Modelling Simul. Mater. Sci. Eng.* **15** 237–61

[81] Smith J A, Wills J B, Moores H S, Orr-Ewing A J, Ashfold M N R, Mankelevich Y A and Suetin N V 2002 Effects of NH_3 and N_2 additions to hot filament activated CH_4/H_2 gas mixtures *J. Appl. Phys.* **92** 672–81

[82] Debroy T, Tankala K, Yarbrough W A and Messier R 1990 Role of heat-transfer and fluid-flow in the chemical vapor-deposition of diamond *J. Appl. Phys.* **68** 2424–32

[83] Frenklach M and Wang H 1991 Detailed surface and gas-phase chemical-kinetics of diamond deposition *Phys. Rev.* B **43** 1520–45

[84] Mankelevich Y A, Rakhimov A T and Suetin N V 1996 Two-dimensional simulation of a hot-filament chemical vapor deposition reactor *Diamond Relat. Mater.* **5** 888–94

[85] Dandy D S and Coltrin M E 1994 Effects of temperature and filament poisoning on diamond growth in hot-filament reactors *J. Appl. Phys.* **76** 3102–13

[86] Mankelevich Y A, Ashfold M N R and Orr-Ewing A J 2007 Measurement and modeling of $Ar/H_2/CH_4$ arc jet discharge chemical vapor deposition reactors II: modeling of the spatial dependence of expanded plasma parameters and species number densities *J. Appl. Phys.* **102** 063310

[87] Kostiuk S V, Mankelevich Y A, Rakhimov A T and Suetin N V 1997 Two-dimensional simulation of diamond deposition processes in microwave discharge reactors *Proc. 5th Int. Symp. on Diamond Materials, The Electrochem. Soc. (Paris, France)* ed J L Davidson *et al* pp 152–60

[88] Hassouni K, Grotjohn T A and Gicquel A 1999 Self-consistent microwave field and plasma discharge simulations for a moderate pressure hydrogen discharge reactor *J. Appl. Phys.* **86** 134–51

[89] Kostiuk S V, Mankelevich Y A, Rakhimov A T and Suetin N V 2000 Reactive mixture activation by dc and mw discharges: two-dimensional simulation *Proc. Physics and Technology Inst. (Moscow, Nauka, Fizmatlit)* vol 16, pp 38–47

[90] Gorbachev A M, Koldanov V A and Vikharev A L 2001 Numerical modeling of a microwave plasma CVD reactor *Diamond Relat. Mater.* **10** 342–6

[91] Yamada H, Chayahara A and Mokuno Y 2007 Simplified description of microwave plasma discharge for chemical vapor deposition of diamond *J. Appl. Phys.* **101** 063302

[92] Mankelevich Y A and May P W 2007 New insights into the mechanism of CVD diamond growth: single crystal diamond in MW PECVD reactors *Diamond Relat. Mater.* **17** 1021–8

[93] May P W, Harvey J N, Smith J A and Mankelevich Y A 2006 Reevaluation of the mechanism for ultrananocrystalline diamond deposition from $Ar/CH_4/H_2$ gas mixtures *J. Appl. Phys.* **99** 104907

[94] May P W and Mankelevich Y A 2008 From ultrananocrystalline diamond to single crystal diamond growth in hot filament and microwave plasma-enhanced CVD reactors: a unified model for growth rates and grain sizes *J. Phys. Chem.* C **112** 12432–41

[95] Lombardi G, Hassouni K, Stancu G D, Mechold L, Ropcke J and Gicquel A 2005 Modeling of microwave discharges of H_2 admixed with CH_4 for diamond deposition *J. Appl. Phys.* **98** 053303

[96] Fox O J L, Ma J, May P W, Ashfold M N R and Mankelevich Y A 2009 The role of inert gas in mw-enhanced plasmas for the deposition of nanocrystalline diamond thin films *Diamond Relat. Mater.* **18** 750–8

[97] Hassouni K, Leroy O, Farhat S and Gicquel A 1998 Modeling of H_2 and H_2/CH_4 moderate-pressure microwave plasma used for diamond deposition *Plasma Chem. Plasma Proc.* **18** 325–62

[98] Hassouni K, Gicquel A, Cappelli M and Loureiro J 1999 Chemical kinetics and energy transfer in moderate pressure H_2 plasmas used in diamond MPACVD processes *Plasma Sources Sci. Technol.* **8** 494–512

[99] Sternschulte H, Bauer T, Schreck M and Stritzker B 2006 Comparison of MWPCVD diamond growth at low and high process gas pressures *Diamond Relat. Mater.* **15** 542–7

[100] Li X L, Perkins J, Collazo R, Nemanich R J and Sitar Z 2006 Investigation of the effect of the total pressure and methane concentration on the growth rate and quality of diamond thin films grown by MPCVD *Diamond Relat. Mater.* **15** 1784–8

[101] May P W, Ashfold M N R and Mankelevich Y A 2007 Microcrystalline, nanocrystalline, and ultrananocrystalline diamond chemical vapor deposition: experiment and modeling of the factors controlling growth rate, nucleation, and crystal size *J. Appl. Phys.* **101** 053115

[102] Bogdan G, Nesladek M, D'Haen J, Maes J, Moshchalkov V V, Haenen K and D'Olieslaeger M 2005 Growth and characterization of near-atomically flat, thick homoepitaxial CVD diamond films *Phys. Status Solidi* a **202** 2066–72

[103] Tallaire A, Achard J, Secroun A, De Gryse O, De Weerdt F, Barjon J, Silva F and Gicquel A 2006 Multiple growth and characterization of thick diamond single crystals using chemical vapour deposition working in pulsed mode *J. Cryst. Growth* **291** 533–9

[104] Vanenckevort W J P, Janssen G, Vollenberg W, Chermin M, Giling L J and Seal M 1991 Thermal chemical vapor-deposition of homoepitaxial diamond—dependence of surface-morphology and defect structure on substrate orientation *Surf. Coat. Technol.* **47** 39–50

[105] Wild C, Herres N and Koidl P 1990 Texture formation in polycrystalline diamond films *J. Appl. Phys.* **68** 973–8

[106] Clausing R E, Heatherly L, Horton L L, Specht E D, Begun G M and Wang Z L 1992 Textures and morphologies of chemical vapor deposited (CVD) diamond *Diamond Relat. Mater.* **1** 411–5

[107] Silva F, Bonnin X, Achard J, Brinza O, Michau A and Gicquel A 2008 Geometric modeling of homoepitaxial CVD diamond growth: I. The {100}{111}{110}{113} system *J. Cryst. Growth* **310** 187–203

[108] Pate B B, Waclawski B J, Stefan P M, Binns C, Ohta T, Hecht M H, Jupiter P J, Shek M L, Pierce D T, Swanson N, Celotta R J, Rossi G, Lindau I and Spicer W E 1983 The diamond (111) surface—a dilemma resolved *Physica* B+C **117** 783–5

[109] Wei J and Yates J T 1995 Diamond surface chemistry.1. A review *Crit. Rev. Surf. Chem.* **5** 1–71

[110] Mayne A J, Riedel D, Comtet G and Dujardin G 2006 Atomic-scale studies of hydrogenated semiconductor surfaces *Prog. Surf. Sci.* **81** 1–51

[111] D'Evelyn M P 1998 Surface properties of diamond *Handbook of Industrial Diamonds and Diamond Films* ed M A Prelas, G Popovici and L K Biglow (New York: Dekker) pp 89–146
[112] Pate B B 1986 The diamond surface—atomic and electronic-structure *Surf. Sci.* **165** 83–142
[113] Thoms B D, Owens M S, Butler J E and Spiro C 1994 Production and characterization of smooth, hydrogen-terminated diamond C(100) *Appl. Phys. Lett.* **65** 2957–9
[114] Thoms B D and Butler J E 1995 HREELS and LEED of H/C(100)—the 2 × 1 monohydride dimer row reconstruction *Surf. Sci.* **328** 291–301
[115] Bobrov K, Mayne A, Comtet G, Dujardin G, Hellner L and Hoffman A 2003 Atomic-scale visualization and surface electronic structure of the hydrogenated diamond C(100)-(2 × 1):H surface *Phys. Rev.* B **68** 195416
[116] Krasnoperov L N, Kalinovski I J, Chu H N and Gutman D 1993 Heterogeneous reactions of H-atoms and CH_3 radicals with a diamond surface in the 300–1133-K temperature-range *J. Phys. Chem.* **97** 11787–96
[117] Cheesman A, Harvey J N and Ashfold M N R 2008 Studies of carbon incorporation on the diamond {100} surface during chemical vapor deposition using density functional theory *J. Phys. Chem.* A **112** 11436–48
[118] Garrison B J, Dawnkaski E J, Srivastava D and Brenner D W 1992 Molecular-dynamics simulations of dimer opening on a diamond (001)(2 × 1) surface *Science* **255** 835–8
[119] Battaile C C, Srolovitz D J and Butler J E 1998 Atomic-scale simulations of chemical vapor deposition on flat and vicinal diamond substrates *J. Cryst. Growth* **194** 353–68
[120] Battaile C C, Srolovitz D J and Butler J E 1997 A kinetic Monte Carlo method for the atomic-scale simulation of chemical vapor deposition: application to diamond *J. Appl. Phys.* **82** 6293–300
[121] Skokov S, Weiner B and Frenklach M 1994 Elementary reaction-mechanism for growth of diamond(100) surfaces from methyl radicals *J. Phys. Chem.* **98** 7073–82
[122] Harris S J 1990 Mechanism for diamond growth from methyl radicals *Appl. Phys. Lett.* **56** 2298–300
[123] Harris S J and Goodwin D G 1993 Growth on the reconstructed diamond (100) surface *J. Phys. Chem.* **97** 23–8
[124] Koleske D D, Gates S M, Thoms B D, Russell J N and Butler J E 1994 Isothermal desorption of hydrogen from polycrystalline diamond films *Surf. Sci.* **320** L105–11
[125] Bobrov K, Mayne A J, Hoffman A and Dujardin G 2003 Atomic-scale desorption of hydrogen from hydrogenated diamond surfaces using the STM *Surf. Sci.* **528** 138–43
[126] Frenklach M and Skokov S 1997 Surface migration in diamond growth *J. Phys. Chem.* B **101** 3025–36
[127] Battaile C C and Srolovitz D J 2002 Kinetic Monte Carlo simulation of chemical vapor deposition *Annu. Rev. Mater. Res.* **32** 297–319
[128] Coltrin M E and Dandy D S 1993 Analysis of diamond growth in subatmospheric dc plasma-gun reactors *J. Appl. Phys.* **74** 5803–20
[129] Netto A and Frenklach M 2005 Kinetic Monte Carlo simulations of CVD diamond growth—interlay among growth, etching, and migration *Diamond Relat. Mater.* **14** 1630–46
[130] Battaile C C, Srolovitz D J, Oleinik I I, Pettifor D G, Sutton A P, Harris S J and Butler J E 1999 Etching effects during the chemical vapor deposition of (100) diamond *J. Chem. Phys.* **111** 4291–9
[131] Battaile C C, Srolovitz D J and Butler J E 1997 Morphologies of diamond films from atomic-scale simulations of chemical vapor deposition *Diamond Relat. Mater.* **6** 1198–206
[132] Battaile C C, Srolovitz D J and Butler J E 1997 Molecular view of diamond CVD growth *J. Electron. Mater.* **26** 960–5
[133] Srolovitz D J, Dandy D S, Butler J E, Battaile C C and Paritosh 1997 The integrated multiscale modeling of diamond chemical vapor deposition *JOM—J. Miner. Met. Mater. Soc.* **49** 42–7
[134] Battaile C C, Srolovitz D J and Butler J E 1999 Point defect incorporation during diamond chemical vapor deposition *J. Mater. Res.* **14** 3439–46
[135] Grujicic M and Lai S G 1999 Atomistic simulation of chemical vapor deposition of (111)-oriented diamond film using a kinetic Monte Carlo method *J. Mater. Sci.* **34** 7–20
[136] Grujicic M and Lai S G 2000 Multi-length scale modeling of CVD of diamond—part II—a combined atomic-scale/grain-scale analysis *J. Mater. Sci.* **35** 5371–81
[137] Brown R C and Roberts J T 2000 Microstructure evolution in diamond CVD: computer simulations of 111 surface site formation on a growing diamond-100 surface *J. Phys. Chem.* B **104** 8420–9
[138] Stallcup R E, Villarreal L M, Lim S C, Akwani I, Aviles A F and Perez J M 1996 Atomic structure of the diamond (100) surface studied using scanning tunneling microscopy *J. Vac. Sci. Technol.* B **14** 929–32